http://dx.doi.org/10.1016/j.jmatprotec.2018.02.021

Formability limits and process window based on fracture analysis of 5A02-O aluminium alloy in splitting spinning

M. Zhan [1*], J. Guo [1], M.W. Fu [2], P.F. Gao [1], H. Long[3], F. Ma [4]

[1] State Key Laboratory of Solidification Processing, School of Materials Science and Engineering, Northwestern Polytechnical University, Xi'an 710072, China

[2] Department of Mechanical Engineering, The Hong Kong Polytechnic University, Hung Hom, Kowloon, Hong Kong

[3] Department of Mechanical Engineering, The University of Sheffield, Sheffield S1 3JD, UK

[4] Long March Machinery Factory, China Aerospace Science and Technology Corporation, Chengdu, 610100, China

*Corresponding author: Mei Zhan, Email: zhanmei@nwpu.edu.cn

Abstract

Splitting spinning or rotary flow splitting is an advanced forming process for manufacturing axisymmetric integrated parts with bifurcated features and unique characteristics of high-performance and low-weight. During the process, under the kinematic effects of mandrel rotational movement and roller radial feed, plastic deformation occurs accompanied usually by undesirable fracture, which restricts the formability limit (FL). In this study, the kinematic effects on the FL of a 5A02-O aluminium alloy in the splitting spinning process were systematically investigated by finite element simulation based on a modified Lemaitre criterion and physical experiments. The results show that at a given roller feed speed or mandrel rotational speed (forming speed), the FL has a nonlinear relationship with forming speed, which increases firstly and then decreases. With the increase of forming speed, the maximum FL decreases and appears at the larger forming speed. These variations of FL show that there exists a combined effect of the roller feed speed and mandrel rotational speed, thus a ratio between them, named as the roller feed ratio, is then used to investigate FL. It is found that there exists a critical roller feed ratio of approximately 2 mm/rev, independent of the speeds of roller and mandrel. Below the critical value, the FL increases with the roller feed ratio increasing. While over the critical value, the FL decreases. In addition, this decrease in FL becomes more remarkable with mandrel rotational speed increasing. Furthermore, variations of stress triaxiality and tensile plastic strain were analyzed to see their effects on the FL. The analyses show that the decrease in tensile plastic strain with the increasing roller feed ratio is dominant the increase of FL below the critical roller feed ratio value. The increase in the stress triaxiality is dominant the decrease of FL when the roller feed ratio is over the critical value in combination with not too high forming speed, whereas both increases are dominant the decrease in FL when it is over the critical roller feed ratio value in combination with high forming speed. Based on the kinematic effects of mandrel and roller, the process windows of the splitting spinning process were obtained to improve the FL. It is found that under the condition of the roller feed ratio within 1-2.5 mm/rev, the mandrel rotational speed within 8-100 rev/min and the roller feed speed within 0.5-4 mm/s are helpful to get high FL values. The experiments were carried out to verify the prediction on the FL and the process window. The research provides an in-depth understanding of FL and its affecting factors, and thus lays a basis for process optimization and process parameter configuration.

Keywords: Splitting spinning; Forming limit; Modified Lemaitre criterion; Kinematic effects; Process window.

1. Introduction

Branched structures have been widely used in many industrial clusters including aviation, aerospace, automotive, railway and energy industries for their high-performance, light-weight and good-property. To efficiently produce the structured components, Groche et al. (2007a) introduced a “linear flow splitting” to manufacture linear “Y” shaped parts, which enables an efficient production of one-piece branched profiles of structured components. For manufacture of V-pulleys, dynamic dampers and automobile wheels, axisymmetric bifurcated preforms with flange on both sides are required (Packham, 1978). Therefore, the “rotary flow splitting” or “splitting spinning” process is thus needed to be developed. The initial researches on splitting spinning process can be found in the 1990’s (Grotmann, 1990). In splitting spinning process, a disk blank is clamped between two mandrels and rotates synchronously with the mandrels. With the radial feed of one or more rollers, the disk blank is split into branch structures with “Y” shape flange, as shown in Fig. 1. The splitting spinning process has the advantages of high process flexibility, good part quality, small equipment capacity and low cost (Huang et al., 2014). The process is thus widely used to manufacture entire wheels, pulley components and the parts with Y-shape features.

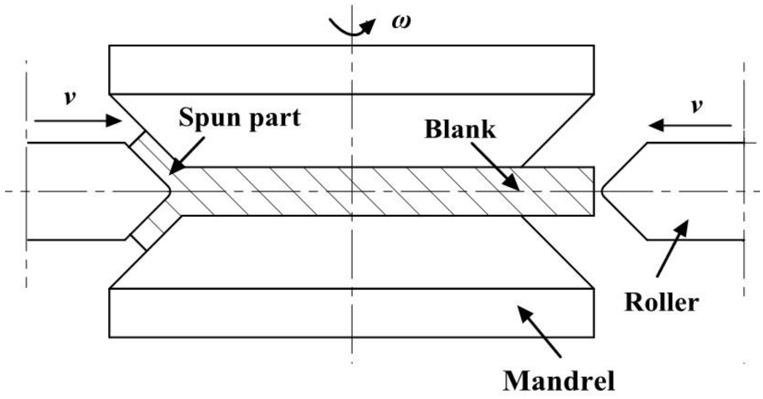

Fig. 1 Schematic illustration of the splitting spinning process.

To develop an efficient splitting spinning process, many researches have been conducted. Prior investigations are more focused on process design principle, forming characteristics and deformation behaviors of materials in flow splitting processes, including linear flow splitting and splitting spinning. Groche et al. (2007b) articulated the process design principle of linear flow splitting process and developed a tool system. With this tool system, the forming characteristics of material flow were studied by experiments. With the aid of finite element (FE) simulation, Müller et al. (2007) analysed the stress and strain distributions in the linear flow splitting process. The compressive stress and the largest plastic strain were identified in the contact zone between splitting roll and metal sheet and the obvious stress and strain gradients were also observed between the contact and non-contact zones. In addition, Schmitt et al. (2012) introduced the development of the linear splitting process for manufacturing sheet metal parts with non-constant cross-sections and optimized the process parameters to control the inhomogeneous deformation. For the splitting spinning process, Schmoeckel and Hauk (2000) described the process in detail and studied the tooling system and process control techniques. Hauk et al. (2000) conducted FE simulation of splitting spinning processing of an AlMgSil (w) material using an axisymmetric FE model and a simplified three-dimensional (3D) FE model. Using these models, the different process parameters (radii of disk blank, blank materials and friction) were seen to lead to obvious changes in forming forces while almost no changes in metal flow. Huang et al. (2008a) simulated the splitting spinning process and the stress and strain were observed to be mainly concentrated in the contact zone between workpiece and roller. The distributions of stress and strain were also non-uniform in the contact and non-contact zones. In addition, Huang et al. (2008b) studied the effects of material parameters on the spinning process of aluminium alloy and the inhomogeneous deformation of material was found to increase with the decrease of yield stress and hardening exponent of the material. Furthermore, Huang et al. (2008c) developed a formula to determine the splitting spinning force with the forming parameters based on the principal stress method. They also analysed the forming characteristics of the process according to the behaviors of roller and concluded that the variation of friction coefficient between contact surfaces would affect the inhomogeneous deformation (Huang et al., 2009).

Splitting spinning is good at manufacturing the axisymmetric bifurcated structures with large flange and thus the large radial depth and high formability limit (FL) are often required. However, the blank experiences complicated plastic deformation in the process with the characteristics of strong inhomogeneous deformation, asymmetry and non-steady state (Huang et al., 2008a). Fracture can easily occur and thus affects the FL of the splitting spinning process. With the rotation of mandrels and radial feed of roller in the process, material flow is strongly affected by the kinematic effects of mandrel and roller (Huang et al., 2009), which would also affect the FL. The so-called FL in this research is considered to be only affected by fracture in splitting spinning. To improve the FL in splitting spinning process, it is important to investigate the kinematic effects of mandrel and roller on material fracture in the process. However, as splitting spinning is such a complicated process with the geometrical, material and boundary nonlinearities, it is difficult, if not impossible, to accurately predict fracture occurrence only by physical experiment and thus FE simulation and physical experiments need to be concurrently employed for the study.

Currently, FE simulation with built-in ductile fracture criteria (DFC) has been proven to be an efficient method to predict fracture and FL in sheet metal forming (Xu et al., 2015), bulk metal forming (Shang et al., 2017) and micro metal forming (Ran et al., 2014) processes. As well known, the DFCs have been divided in two types. One type is the uncoupled DFCs (without considering the damage evolution in material constitutive model), including the C&L, Oyane, Brozzo, Rice-Tracey and Mohr-Coulomb DFCs. These DFCs were used to predict the FL in three-point bending (Song et al., 2005), hydro forming process (Mashayekhi et al., 2007), hole expanding process (Ko et al., 2007), panel bending (Yan et al., 2011) and single point incremental forming (Mirnia and Shamsari, 2017) processes with FE simulation successfully. The other type is the coupled DFCs (regarding the damage evolution in material constitutive model), including the Lemaitre DFC (Malcher and Mamiya, 2014). The Lemaitre DFC has been employed in the hemispherical punch bulging (Liu et al., 2009) and hot stamping (Tang et al., 2016) and the results indicated that the Lemaitre DFC has a better agreement with experiment than that of other uncoupled DFCs in predicting FL. In terms of spinning process, Ma et al. (2015) used several uncoupled DFCs to numerically simulate the tube-spinning process and concluded that the C&L's DFC provides the most accurate prediction of FL. Zhan et al. (2009) adopted the Lemaitre DFC and the C&L's DFC in the FE simulation of splitting spinning process. Their results showed that the Lemaitre DFC is better than the C&L's one in predicting fracture occurrence and distribution in the process, which is different from the conclusion by Ma et al. (2015). This difference is due to that the damage evolution is incorporated in the material constitutive model when the Lemaitre DFC is used, which makes the damage prediction more accurate on one hand. On the other hand, the difference is also attributed to different loadings and deformation modes of these two spinning processes. Though the Lemaitre DFC provided better prediction in FL than the C&L DFC did in the splitting spinning process, there still exists a large difference from the experiment to use the Lemaitre DFC. This Lemaitre DFC was established based on the linear relationship between the damage value and plastic strain, which is presented by most metals. While for the aluminium alloy, a nonlinear relationship was found by Chow and Wang, (1987) for a Al2024 alloy, and a nonlinear Lemaitre DFC was established based on this nonlinear relationship (Bonora, 1997a). Similarly, the nonlinear relationship was also observed by Wu et al. (2011) for a 5A02 alloy. Thus, considering this nonlinear relationship, Wu et al. (2011) modified the Lemaitre DFC by introducing a new non-linearity function to replace the linearity one to model the damage evolution and to give more accurate prediction. Their results showed that the prediction using the modified Lemaitre DFC is more consistent with the experimental results in terms of fracture prediction and thus the modified one is good at predicting the fracture and FL in the splitting spinning process of aluminium alloy.

The successful prediction of fracture and FL in the above review demonstrates that FE simulation using an efficient DFC is able to predict the FL in forming process. However, the prior arts are more focused on the prediction of fracture occurrence and damage distribution, whereas the kinematic effects of mandrel and roller on FL in splitting spinning process and the FL variation reasons under these conditions have not yet been considered.

In this study, the kinematic effects of mandrel rotational and roller feed speeds on the FL of 5A02-O aluminium alloy in splitting spinning process were systematically investigated by FE simulation using a modified Lemaitre criterion. The responsible factors for FL variation under different forming conditions were thoroughly explored and discussed. Based on the understanding established via these explorations, the optimized process window of mandrel and roller to achieve high good formability and high FL were determined. The efficiency of the optimized process window was further validated and corroborated by experiments and thus the research provides a solution for improving the formability of splitting spinning process for industries.

2. Numerical investigation methods

To investigate the kinematic effects of mandrel rotational and roller radial speeds on FL in the splitting spinning process, DFC-based FE simulation of the process was conducted. With the help of the simulation, the instantaneous deformation and damage of material during the process can be obtained, which is generally very difficult and even impossible by physical experiment (Fu, 2016).

2.1 Modified Lemaitre criterion

The original Lemaitre criterion was established based on continuum damage mechanics, and its incremental form is designated by Eq. (1) (Lemaitre, 1985),

$$\Delta D = \frac{D_C}{\varepsilon_R - \varepsilon_D}\left[\frac{2}{3}(1+\nu)+3(1-2\nu)\left(\frac{\sigma_m}{\overline{\sigma}}\right)^2\right]\left(\frac{\sigma}{K}\right)^2\Delta\varepsilon \tag{1}$$

where ε_D, ε_R and D_C are the plastic strain at the onset of damage, the plastic strain at fracture and the critical damage value at fracture, respectively. In addition, ν is Poisson ratio, K is strength coefficient, σ is flow stress, σ_m is hydrostatic stress, $\overline{\sigma}$ is the equivalent stress and $\Delta\varepsilon$ is the plastic strain increment. The ratio of hydrostatic and equivalent stresses, i.e., $\sigma_m / \overline{\sigma}$, termed as stress triaxiality, represents the triaxial state of stress and describes the progressive decrease in material ductility under increasing triaxial state of stress (Li et al., 2011).

In this study, a modified Lemaitre criterion designated in Eq. (2) was used,

$$\Delta D = \left\{ \mathrm{g}'(\varepsilon)\left[\frac{2}{3}(1+\nu)+3(1-2\nu)\left(\frac{\sigma_m}{\overline{\sigma}}\right)^2\right]\left(\frac{\sigma}{K}\right)^2\Delta\varepsilon \right. \tag{2}$$

where $\mathrm{g}'(\varepsilon)$ is a non-linearity function representing the variation slope between the damage value and the plastic strain. The original function of $\mathrm{g}'(\varepsilon)$ is $\mathrm{g}(\varepsilon)$. This modified Lemaitre criterion was developed by the author's research group based on the nonlinear relationship between the damage value and plastic strain (Wu. et al., 2011 and Bonora, 1997b).

To apply the modified Lemaitre criterion, the damage constants (ε_R, ε_D, and D_c), the function $g(\varepsilon)$ and its derivative $g'(\varepsilon)$, which are closely related to the material, should be determined. In previous researches, the constants were usually determined by measuring the variations of Young's modulus $\tilde{E}$ in the uniaxial tension tests (Lemaitre, 1985). With the tension tests, the damage constants in the Lemaitre criterion were determined and used in different tensile tests with various stress triaxialities (Lemaitre, 1985), the tube bending (Li et al., 2011) and hot stamping (Tang et al., 2016) with good fracture prediction accuracy. Thus, in this research, the uniaxial tension test was adopted by measuring the variation of Young's modulus $\tilde{E}$, as shown in Eq. (3),

$$D = 1 - \frac{\tilde{E}}{E} \tag{3}$$

where E is the original Young's modulus, while $\tilde{E}$ is the Young's modulus at different deformation stages. The variation of Young's modulus can be measured by repetitive loading-unloading test, as shown in Fig. 2. The repetitive loading-unloading tensile test was carried out on a CMT5205 electronic universal testing machine. Sheet sample was used in this test and was cut from the circular blank. In the testing, the loading velocity was set as 1 mm/min and the unloading process was conducted when loading displacement reached 1mm. In the unloading process, it was controlled by force and the decreasing force speed is 10 N/s. The repetitive loading-unloading cycle was set as 16. The Young's moduli at different deformation stages were obtained by measuring the unloading slope for better accuracy. The laser extensometer with the accuracy of 0.001 mm was used in the test to guarantee the accuracy of the Young's modulus.

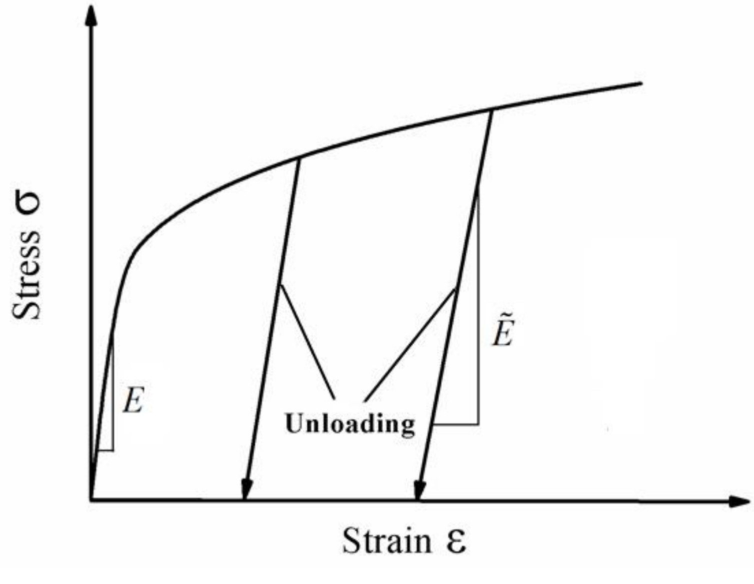

Fig. 2 Sketch of the repetitive loading-unloading test.

In this research, the 5A02-O aluminium alloy, viz., AlMg2.5 in International Standard was used. Its chemical compositions and material properties are listed in Tables 1 and 2, respectively. The isotropic hardening material model was used to show the mechanical behavior of this alloy, as shown in Eq. (4),

$$\sigma = K\varepsilon^n \tag{4}$$

where σ is the flow stress, K is the strength coefficient and n is the hardening exponent. The values of these parameters are the same as those in Table 2.

Table 1: Chemical composition of 5A02-O aluminum alloy.

Element	Al	Mg	Mn	Fe	Si	Ti	Cu
Content wt%	Matrix	2.5	0.21	0.22	0.15	0.1	0.08

Table 2: Material parameters of 5A02-O aluminium alloy blank.

Density/ ($Kg.m^{-3}$)	Original elastic modulus/GPa	Yield strength/MPa	Strength coefficient/MPa	Poisson's ratio	Hardening exponent
2680	70.3	90.0	275.0	0.3	0.16

For the 5A02-O aluminium alloy, the Young's moduli at different deformation stages are shown in Fig. 3(a). The relationship between the damage variable D and plastic strain ε was obtained according to the change of Young's modulus, as shown in Fig. 3(b). In this figure, the damage shows a nonlinear relationship with the plastic strain. At the beginning stage, after a very limited plastic strain (around 0.025), the damage value already reaches 0.12 (almost 70% of critical damage value) and then has a relatively slow increase trend. This damage evolution trend is different with that in most metals (such as copper and steel), while the same as that in the Al2024 aluminium alloy clarified by Chow and Wang, (1987). This is due to that in the aluminium alloy, the damage evolution is dominated by the nucleation phase (Bonora, 1997a and Bonora et al., 1996). Many voids are nucleated when a small threshold strain is reached. Thus, the damage increases rapidly at the beginning stage. Further increase of strain produces an additional number of micro voids with a very limited growth of the already formed voids, which results in the slow increase of damage. Till this process is saturated and the void spacing is highly reduced, the void coalescence occurs and leads to fracture.

By fitting the relationship between damage and plastic strain, $\mathrm{g}(\varepsilon)$ was obtained (Eq. (5)), and $\mathrm{g}'(\varepsilon)$ was derived (Eq. (6)).

$$\mathrm{g}(\varepsilon)=0.511-0.392\mathrm{e}^{(-\varepsilon/1.907)}-0.119\mathrm{e}^{(-\varepsilon/0.0089)} \tag{5}$$

$$\mathrm{g}'(\varepsilon)=0.2056\mathrm{e}^{(-\varepsilon/1.907)}+13.3708\mathrm{e}^{(-\varepsilon/0.0089)} \tag{6}$$

By letting $\mathrm{g}(\varepsilon)$=0 , ε_D was determined as 0. ε_R was obtained by measuring the strain in uniaxial tension tests when fracture appears. As an extensometer rather than a strain gage was used for strain measurement, the measured true strain was the average value within the gage length. The average value was less than the actual strain when localization occurs. Thus, ε_R could be directly obtained as the maximum plastic strain when fracture appeared by comparing the simulation results with the experimental results in terms of the deformation level at which fracture occurred. For the 5A02-O aluminium alloy, ε_R was determined as 0.3. Furthermore, when letting ε=ε_R in $g(\varepsilon)$, i.e., $D_C=g(\varepsilon_R)$, D_C was obtained as 0.176 .

Considering that when the strain is close to 0.3, the change tendency of damage almost keeps stable (Fig. 3(b)), it is feasible to use Eqs. (2), (5) and (6) to predict the damage evolution at the large strain level over 0.3.

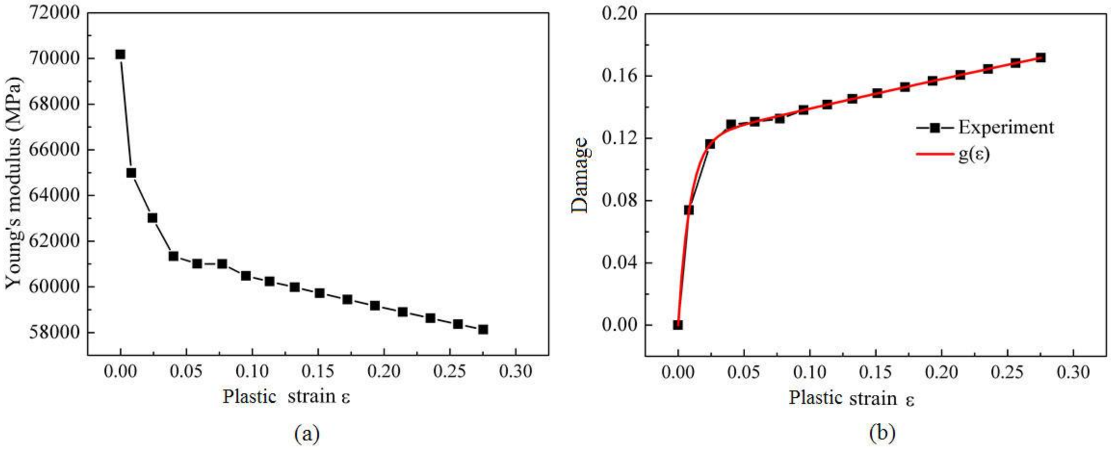

Fig. 3 Variations of Young's modulus and damage at different deformation stages: (a) Young's modulus and (b) damage.

2.2 Development of FE model

In the splitting spinning process, there exists a large plastic deformation with the nonlinearities of material, geometry and boundary, and relatively high strain rate magnitude (about 10 s^{-1}). Thus to describe the deformation behaviors, ABAQUS/ Dynamical, Explicit code was used in this research and a three-dimensional (3D) elastic-plastic FE model was developed, as shown in Fig. 4.

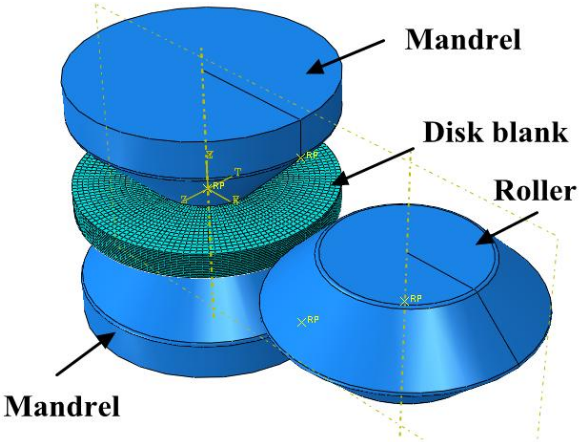

Fig. 4 3D elastic-plastic FE model for splitting spinning.

In the model, the disk was set as a deformable body and meshed by an 8-node reduced integration brick element. Theoretically, the mesh size makes a big difference on the deformation prediction accuracy. The finer the mesh is, the more accurate the deformation prediction is, while the longer computing time required. Thus, to reasonably determine the mesh size, the equivalent plastic strain distribution, time cost and critical feed depth at fracture onset of four FE simulations with the element number of 10, 15, 20 and 25 along the axial direction of the disk blank were compared, as shown in Figs. 5 and 6. In Fig. 5, it can be observed that the equivalent plastic strain values show little difference among the element number of 15, 20 and 25. While the equivalent plastic strain values when using these three element numbers are less than that with the element number of 10. The difference indicates that the element number no less than 15 is accurate enough to predict the deformation in the splitting spinning process. Furthermore, in Fig. 6, it can be seen that when the element number is no less than 15, the critical feed depths show little difference. Thus, considering that the computational time with the element number of 15 is much less than those with the element number of 20 and 25 (Fig. 5), 15 elements were adopted along the axial direction of the disk blank. In addition, the adaptive mesh control was applied to remesh the spun part during the process. The roller and the mandrels were set as rigid body.

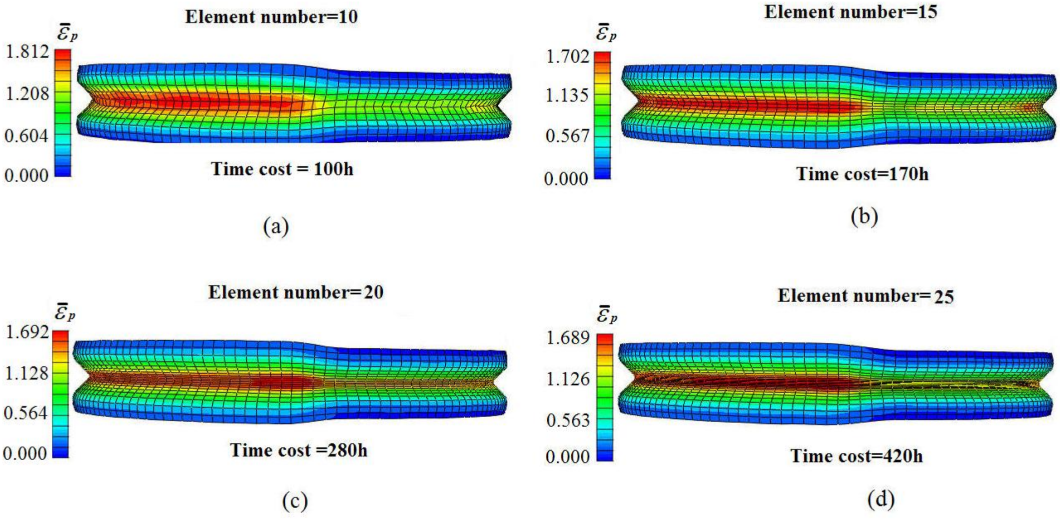

Fig. 5 Equivalent plastic strain distribution and time cost with different element numbers (a) 10, (b) 15, (c) 20 and (d) 25 along the axial direction at the feed depth of 10 mm.

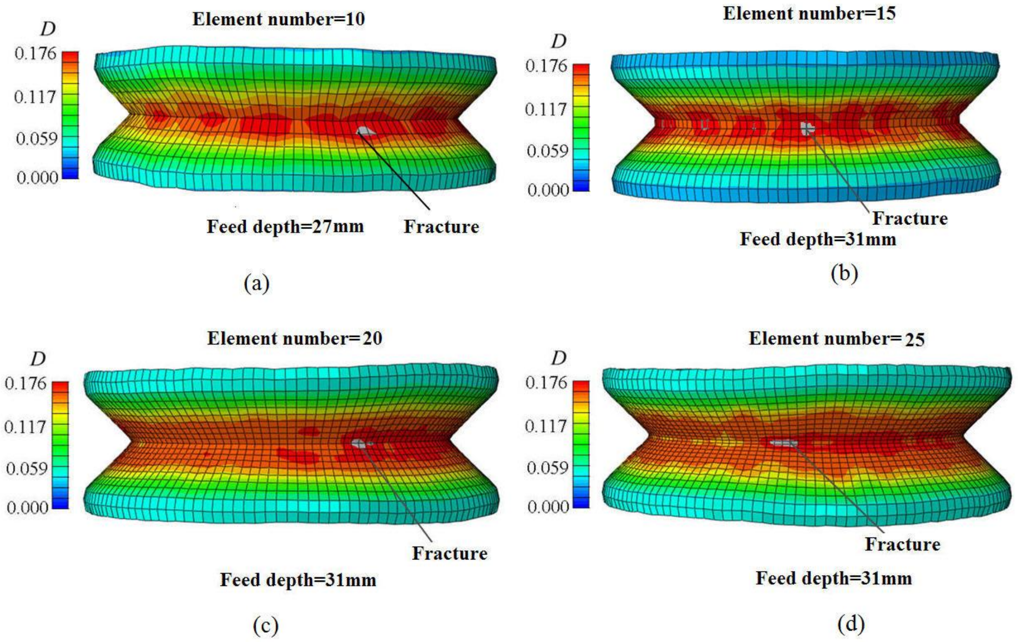

Fig. 6 Critical feed depth at fracture onset with different element numbers (a) 10, (b) 15, (c) 20 and (d) 25 along the axial direction.

In previous researches, the splitting spinning process was simulated with the rotation of the mandrels and axial feed of roller. However, in these models, with the rotation of mandrels, the material would rotate with the mandrels. The imaginary phenomena such as material flow due to the artificial centrifugal effects occur. To avoid these artificial imaginary phenomena, the mandrels keep steady in the FE model, and the disk blank is fixed with the mandrel by applying a 60 KN force on each mandrel. While for the purpose to investigate the kinematic effect of the mandrel, the same mandrel rotation was applied on the roller. Thus, the roller not only feeds radially but also turns around the fixed disk blank like a planetary in the FE model. Furthermore, no mass scaling technique was used in this simulation to avoid the artificial imaginary phenomena.

The contacts in the FE model were all defined as surface-to-surface contact and the penalty contact method was used. The process parameters of FE analysis are listed in Table 3. The friction coefficient between the blank and the splitting roller was set as 0.05 due to the rolling contact between the blank and the splitting roller (Zhao and Li, 2016). In the splitting spinning process, there exist two contacts between the blank and mandrels, as shown in Fig. 7. One is the contact between the end surfaces of two mandrels and blank. The friction coefficient in this contact was defined as 0.5. While the other is the contact between the side surfaces of the two mandrels and the outer surfaces of the spun part flanges. During the forming process, there is a small relative sliding in this contact. Thus, a small coefficient of 0.05 for this contact was chosen in this study.

Table 3: Fundamental parameters of 3D FE analysis for splitting spinning.

Process parameters	Values
Initial diameter of blank (mm)	200.0
Initial thickness of blank (mm)	20.0
Diameter of splitting roller (mm)	200
Splitting angle of splitting roller (degree)	45.0
Round radius of splitting roller (mm)	2.0
Roller feed speed (mm/s)	1.0
Mandrel rotational speed (rev/min)	60
Diameter of mandrel large end (mm)	200.0
Friction coefficient between blank and splitting roller	0.05
Friction coefficient between blank and side surfaces of mandrels	0.05
Friction coefficient between blank and end surfaces of mandrels	0.5

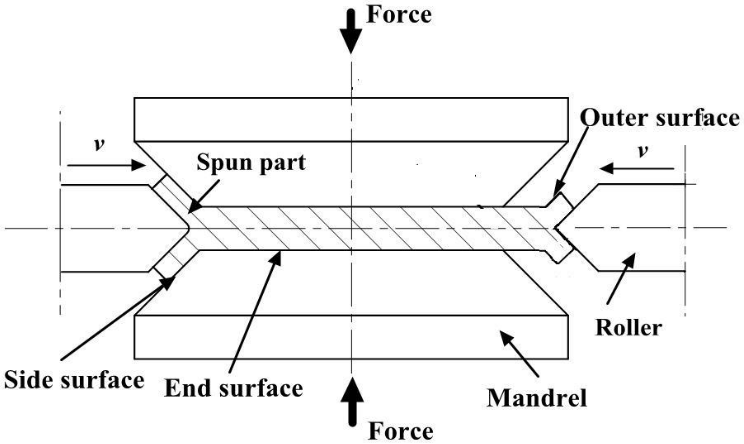

Fig. 7 Illustration of the contact between the workpiece and mandrels.

In addition, the temperature effect was ignored in this study as the coolant was used throughout the spinning process in the experiment in this research. The observation showed that the use of coolant could significantly avoid temperature rise and the temperature was almost maintained at room temperature in the process. Furthermore, the strain rate effect was also ignored in the material model since the strain rate in the process is in the magnitude of 10 s^{-1}, while within the range (0.001-10 s^{-1}) the mechanical responses (flow behavior and fracture behavior) of the aluminium alloy did not have a big difference (Kabirian et al., 2014).

2.3 FE implementation of the modified Lemaitre criterion

The modified Lemaitre criterion described in Section 2.1 was configured based on the uniaxial tension tests, in which the material experiences tensile hydrostatic stress throughout the process. In the splitting spinning process, however, the material experiences tensile and compressive hydrostatic stress. In this research, the tensile and compressive hydrostatic stress states were thus separated in the modified Lemaitre criterion and the damage evolution follows Eqs. (7), (8) and (9),

$$\Delta D = \begin{cases} g'(\varepsilon_{tensile})\left[\frac{2}{3}(1+\nu)+3(1-2\nu)\left(\frac{\sigma_m}{\bar{\sigma}}\right)^2\right]\left(\frac{\sigma}{K}\right)^2 \Delta\varepsilon_{tensile} & {}^{\sigma_m}/_{\bar{\sigma}} \geq 0 \\ 0 & {}^{\sigma_m}/_{\bar{\sigma}} < 0 \end{cases} \tag{7}$$

$$\Delta\varepsilon_{tensile} = \begin{cases} \Delta\varepsilon & {}^{\sigma_m}/_{\bar{\sigma}} \geq 0 \\ 0 & {}^{\sigma_m}/_{\bar{\sigma}} < 0 \end{cases} \tag{8}$$

$$g'(\varepsilon_{tensile}^{N+1}) = \begin{cases} g'(\varepsilon_{tensile}^{N} + \Delta\varepsilon) & {}^{\sigma_m}/_{\bar{\sigma}} \geq 0 \\ g'(\varepsilon_{tensile}^{N}) & {}^{\sigma_m}/_{\bar{\sigma}} < 0 \end{cases} \tag{9}$$

where $\varepsilon_{tensile}$ is the tensile plastic strain, which is the plastic strain under tensile hydrostatic stress, $\Delta\varepsilon_{tensile}$ is the tensile plastic strain increment and N is the increment step number. From Eqs. (7)-(9), it can be seen that when the material experiences tensile hydrostatic stress, the damage accumulates. While the material experiences compressive hydrostatic stress, there is no damage evolution due to the crack closure effect (Bouchard et al., 2011).

The element delete technique was used in the VUMAT subroutine to observe the fracture clearly. The technique was implemented into the VUMAT subroutine based on a solution dependent variable (SDV). As discussed in Section 2.1, the critical damage value at fracture D_C was obtained as 0.176 for the 5A02-O aluminium alloy. Thus when the damage value $D \geq D_C = 0.176$, sets SDV=0, which means the element will be deleted. While $D < D_C = 0.176$, sets SDV=1, which means the element will be remained.

2.4 Division and paths of the deformation zone

In splitting spinning process, the splitting roller rotates around the blank and moves along the radial direction of the blank. The splitting roller presses the blank and causes local plastic deformation. To conveniently describe the damage evolution in the process, three zones were studied in this research, viz., the upcoming deformation area in front of the roller, the deforming area under the action of the roller, and the deformed area behind the roller, as shown in Fig. 8. In this figure, axial paths are selected in each area and named as paths 1, 2 and 3, and a point is also selected at the flange bottom area.

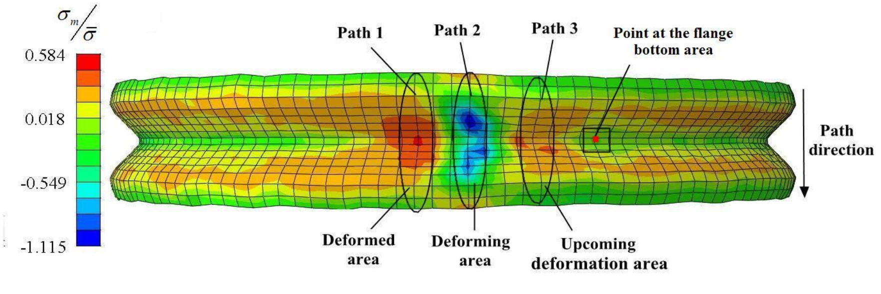

Fig. 8 Deformation zones, paths and point selected for study.

2.5 Damage evolution and fracture occurrence

Using the FE model for the splitting spinning and the process parameters in Table 3, the distributions of stress triaxiality, tensile plastic strain, and the damage at the feed depth of 10 mm were obtained, as shown Fig. 9. In Fig. 9(a), it is revealed that the deforming area is under a negative stress triaxiality state as the material is being deformed under the compression of the roller. While for the upcoming deformation area and the deformed area, they are always under positive stress triaxiality states, and the maximum value of stress triaxiality appears in the flange bottom of these two areas. As the damage increases under the positive stress triaxiality, it can be concluded that the evolution of damage is possible to induce mainly in the upcoming deformation area or the deformed area.

As seen from the distribution of the accumulation of tensile plastic strain (Fig. 9(b)), the maximum value is observed to appear in the deformed area. This is the result of material flow, as shown in Fig. 10. In the figure, the material not only flows in the deforming area, but also flows to the deformed and upcoming deformation areas, which results in the tensile plastic strain in the latter two areas. With the combined effect of stress triaxiality and tensile plastic strain, the maximum damage appears in the deformed area and is located in the flange bottom, as shown in Fig. 9(c).

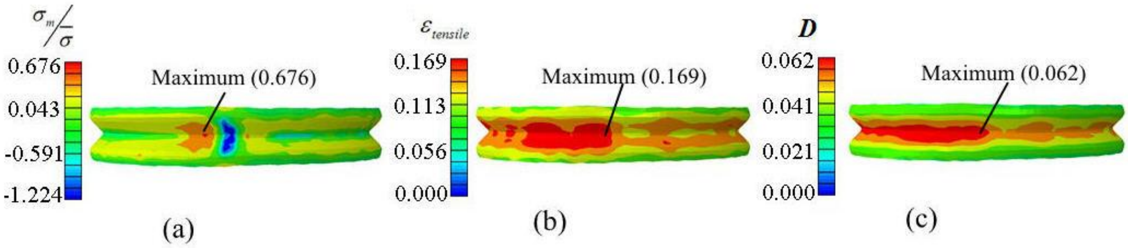

Fig. 9 Distributions of: (a) stress triaxiality, (b) tensile plastic strain and (c) damage at the feed depth of 10mm.

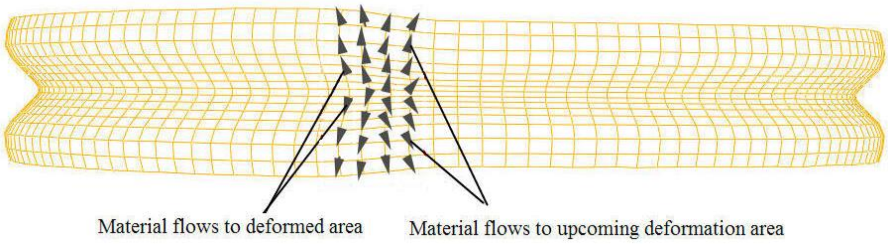

Fig. 10 Material flow in the splitting spinning process.

The distributions of stress triaxiality, tensile plastic strain and damage at different roller feed depths along path 1 in the deformed area are also investigated to study the damage evolution rule in the splitting spinning process, as shown in Fig. 11. In Fig. 11(a), it can be seen that the stress triaxiality show a single-peak distribution and the maximum value appears at the flange bottom. With the increase of feed depth, the value and distribution of stress triaxiality do not have a big difference in the flange bottom area. While in Fig. 11(b), it can be observed that the tensile plastic strain and damage increases with the feed depth and still shows the single-peak distribution. As a result, with the increase of feed depth, the maximum damage appears in the flange bottom and the fracture occurs when the damage achieves the value of D_C, as shown in Fig. 12.

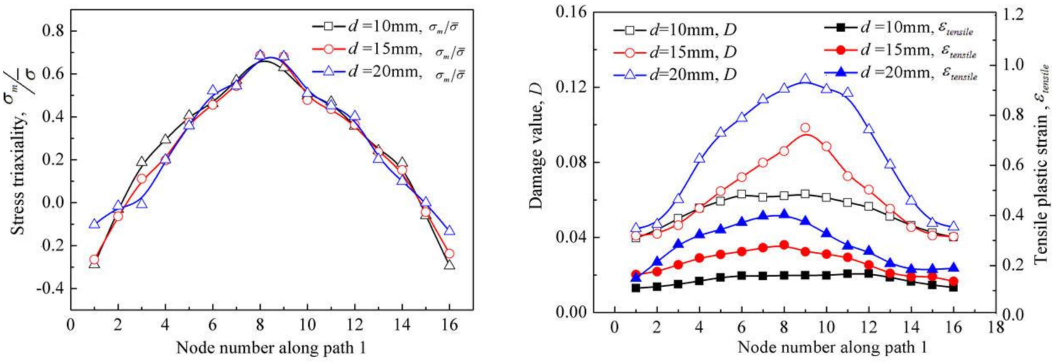

(a) (b)

Fig. 11 Distributions of (a) stress triaxiality and (b) tensile plastic strain and damage along path 1 at different feed depths.

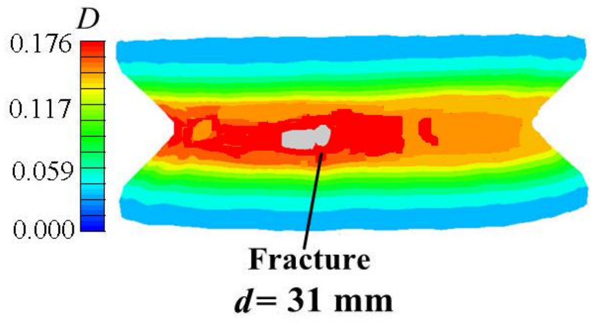

Fig.12 Fracture occurrence at the feed depth (d) of 31mm.

In addition, to investigate the damage evolution in the process one step further, the evolution of stress triaxiality, tensile plastic strain and damage to the feed depth 20mm at the selected point in the flange bottom area (Fig. 8) are shown in Fig. 13. As seen in Fig 13(a), the material experience repetitive negative and positive stress triaxiality, which are caused by the continuous deformation characteristics under the local loading of rollers in the process. Under this changing stress triaxiality history, the tensile plastic strain and damage increases and accumulated discontinuously in the process, as shown in Fig. 13 (b).

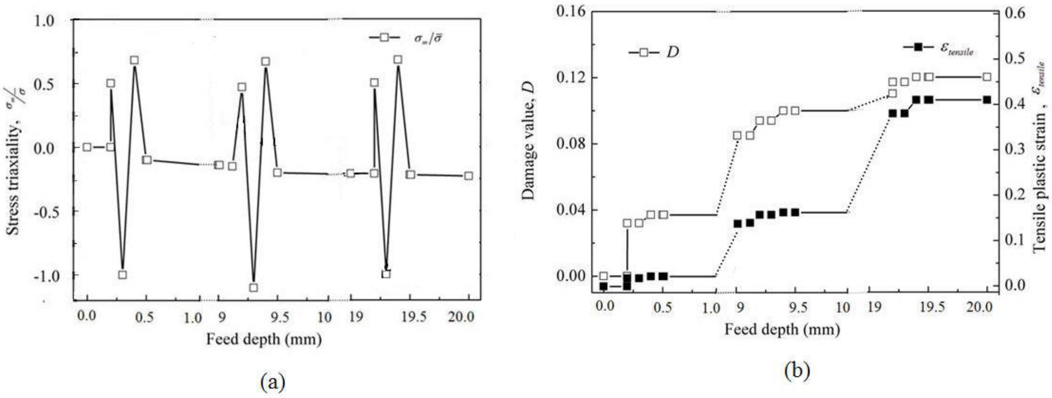

Fig.13 Evolution of (a) stress triaxiality (b) tensile plastic strain and damage to the feed depth of 20 mm at the selected point in the flange bottom area.

3. Kinematic effects of mandrel and roller

In this section, the FL in the splitting spinning process was firstly defined, and the simulation schemes to study the kinematic effects of mandrel and roller on FL were designed. Then, the variations of FL with the mandrel rotational and roller feed speeds were investigated. Furthermore, considering the combined effects of the forming speeds, the variations of FL with the roller feed ratio were explored. Finally, the reasons behind the variations of the FL were analyzed.

3.1 Definition of FL and research scheme

The FL of the splitting spinning process, designated as m_f, is defined as the ratio between *d* and *R* in the following Eq. (10):

$$m_f = d / R \times 100\% \qquad (10)$$

where *d* is the roller feed depth when fracture occurs, i.e., the maximum feed depth, and *R* is the radius of the blank, as shown in Fig. 14. The FL m_f represents the maximal relative deformation extent before the occurrence of fracture. A larger value of m_f indicates a greater FL in splitting spinning process.

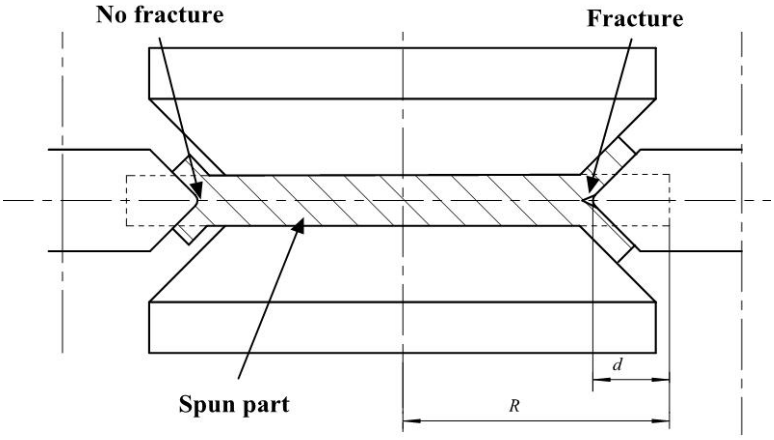

Fig. 14 Sketch of the fracture in splitting spinning.

The mandrel rotational speed determines the relative rotation between the roller and the workpiece. The roller feed speed controls the radial movement of the roller. The roller feed ratio, which is a relative parameter depending on the mandrel rotational and roller feed speeds, is shown in Eq. (11). It decides the relative movement between the material and the roller, i.e., the feed amount of the roller per revolution of the roller.

$$f = v/n_m = \frac{60v}{\omega} \tag{11}$$

In Eq. (11), ω is the revolution of the mandrel per minute (unit: rev/min), n_m is the revolution of the mandrel per second (unit: rev/s), and v is the roller feed speed per second (unit: mm/s).

To study the kinematic effects of mandrel and roller on the FL of splitting spinning process, the simulation schemes for these two parameters are shown in Table 4: When the given roller feed speed v is 0.5, 1 and 2.3 mm/s, the mandrel rotational speed ω changes in the range of 8 to 300 (No. 1-14), 10-300 (No. 15-28) and 25-300 rev/min (No. 29-38), respectively. While when the selected mandrel rotational speed ω is 40 (No. 39-46), 100 (No. 47-56) and 140 rev/min (No. 57-66), v changes in the same range of 1 to 7 mm/s. Other parameters are identical to those in Table 3.

Table 4 Simulation schemes of the splitting spinning process.

No.	1	2	3	4	5	6	7	8	9	10	11	12	13	14
ω	8	10	12	15	20	25	40	50	70	100	140	180	220	300
v	0.5	0.5	0.5	0.5	0.5	0.5	0.5	0.5	0.5	0.5	0.5	0.5	0.5	0.5
No.	15	16	17	18	19	20	21	22	23	24	25	26	27	28
ω	10	15	20	25	30	40	50	70	100	140	180	220	260	300
v	1	1	1	1	1	1	1	1	1	1	1	1	1	1
No.	29	30	31	32	33	34	35	36	37	38				
ω	25	40	50	58	70	100	140	180	220	300				
v	2.3	2.3	2.3	2.3	2.3	2.3	2.3	2.3	2.3	2.3				
No.	39	40	41	42	43	44	45	46						
ω	40	40	40	40	40	40	40	40						
v	1	1.33	1.63	2.3	4	5.5	6.3	7						
No.	47	48	49	50	51	52	53	54	55	56				
ω	100	100	100	100	100	100	100	100	100	100				
v	1	1.63	2.3	3	3.5	4	4.9	5.5	6.3	7				
No.	57	58	59	60	61	62	63	64	65	66				
ω	140	140	140	140	140	140	140	140	140	140				
v	1	1.63	2.3	3	3.5	4	4.9	5.5	6.3	7				

3.2 Effect of mandrel rotational speed

Based on the simulations of No. 1-38 in Table 4, the variation trends of the FL with the mandrel rotational speed at three given roller feed speeds were firstly investigated and shown in Fig. 15. From the figure, it can be seen that, at a given roller feed speed, all FLs tend to increase and subsequently decrease with the increase of mandrel rotational speed. However, with the increase of roller feed speed, the peak value of the FL decreases and appears at the larger mandrel rotational speed. These phenomena indicate that the FL is affected by both the mandrel rotational and the roller feed speeds. Furthermore, in Fig. 15, it can be also observed that, to obtain a high FL, when the mandrel rotation speed is less than 20 rev/min, a small roller feed speed such as 0.5 mm/s is desirable; when the mandrel rotational speed is 20-50 rev/min, a moderate roller feed speed such as 1.0 mm/s is acceptable; while when the mandrel rotation speed is larger than 50 rev/min, a large roller feed speed (such as 2.3 mm/s) is optimal..

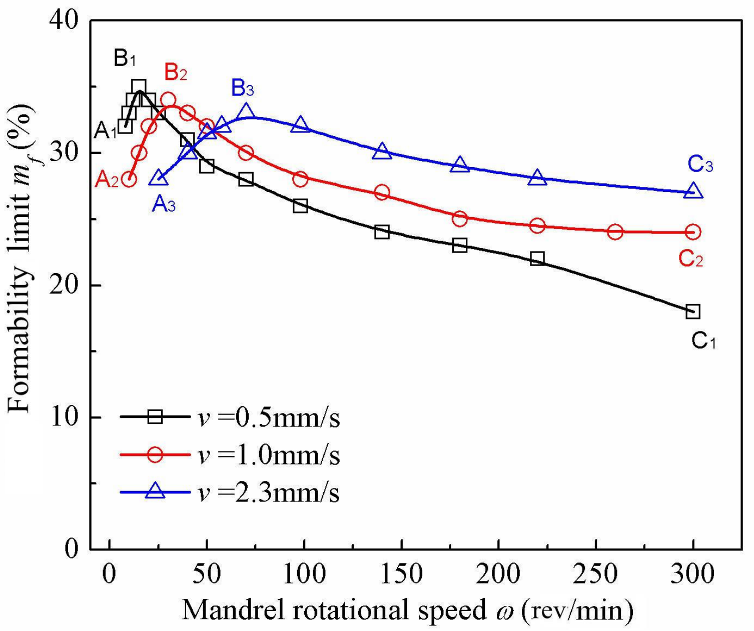

Fig. 15 Effect of the mandrel rotational speed on the FL at different given roller feed speeds.

3.3 Effect of roller feed speed

While based on the simulations of No. 39-66 in Table 4, the variation trends of the FL with the roller feed speed at three given mandrel rotational speeds were investigated and shown in Fig. 16. From the figure, it can be observed that, at a given mandrel rotational speed, the FL also tends to increase and subsequently decrease with the increase of roller feed speed. Similarly, with the increase of mandrel rotational speed, the peak value of the FL decreases a little and appears at a larger roller feed speed. These phenomena also indicate that FL is affected by both the roller feed and mandrel rotational speeds. From Fig. 16, it can be also seen that, to acquire a high FL, when the roller feed speed is less than 2 mm/s, a small mandrel rotational speed such as 40 rev/min is desirable; when the roller feed speed is in the range of 2-4 mm/s, a moderate mandrel rotation speed (such as 100 rev/min) is acceptable; when the roller feed speed is in 4-5.5 mm/s, a large mandrel rotation speed (such as 140 rev/min) is optimal.

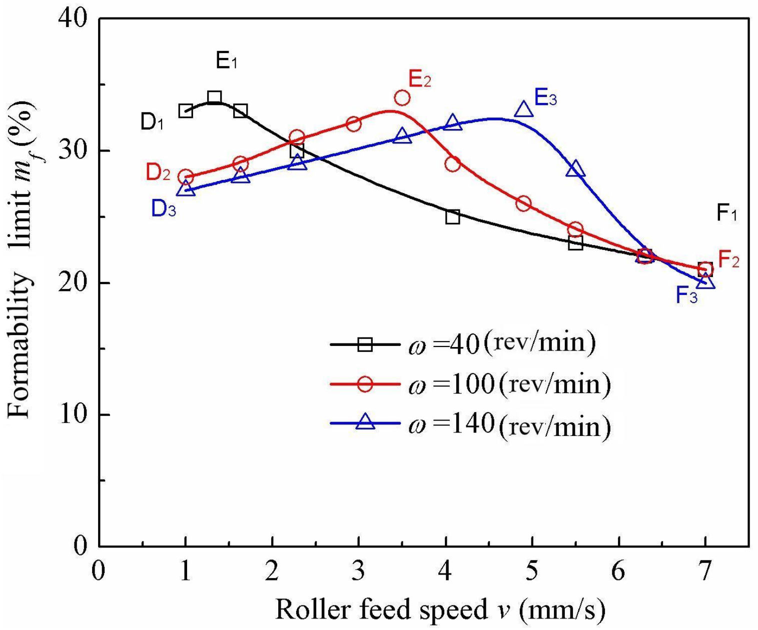

Fig. 16 Effect of the roller feed speed on the FL at different given mandrel rotational speeds.

3.4 Effect of roller feed ratio

As discussed in Sections 3.2 and 3.3, FL is affected by both the roller feed and mandrel rotational speeds. To more clearly investigate their combined effect, the roller feed ratio was introduced (Wang et al., 2011). According to the simulations of No. 1-38 in Table 4, the relationships between the FL and the roller feed ratio at three given roller feed speeds were obtained, as shown in Fig. 17. Furthermore, based on the simulations of No. 39-66 in Table 4, the relationships between the FL and the roller feed ratio at three mandrel rotational speeds were obtained, as shown in Fig. 18.

As seen from Fig. 17, with different given roller feed speeds and an increase of the roller feed ratio, FL tends to increase firstly and then decrease. FL reaches its peak value at a critical roller feed ratio of approximately 2 mm/rev whatever the roller feed speed is. The FL curve under a large given roller feed speed, is lower a little than that under a small roller feed speed.

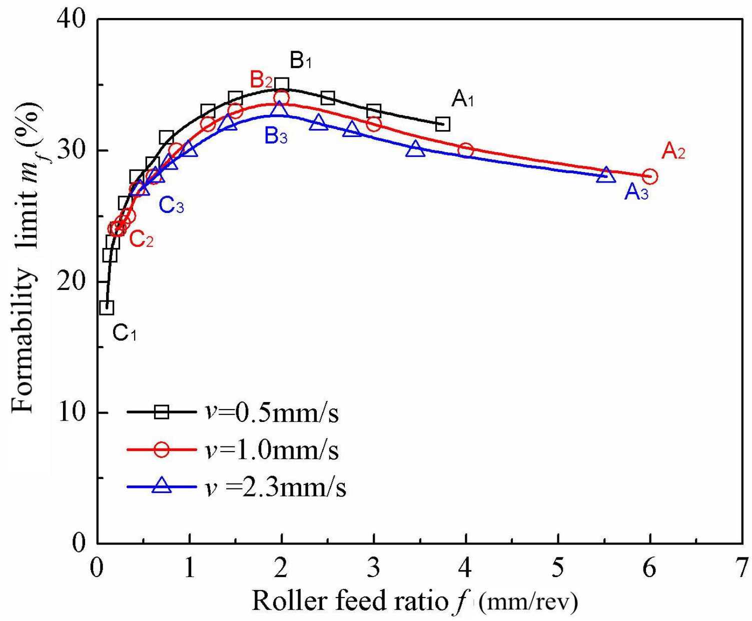

Fig. 17 Effects of the roller feed ratio on the FL at different given roller feed speeds.

From Fig. 18, it can be seen that the FL under a given mandrel rotational speed also increases firstly and is followed by decrease with the increase of the roller feed ratio. The FL reaches its peak value at the same critical roller feed ratio of approximately 2 mm/rev whatever the mandrel rotational speed is. When the roller feed ratio is below the critical value, there is no significant difference in the FL curves under different given mandrel rotational speeds, which is similar to the variation characteristic of the FL under different roller feed speeds. While when the roller feed ratio is higher than the critical value, with the increase of the mandrel rotational speed, the FL curve significantly becomes lower, which is remarkably different from the variation characteristic of the FL under different roller feed speeds.

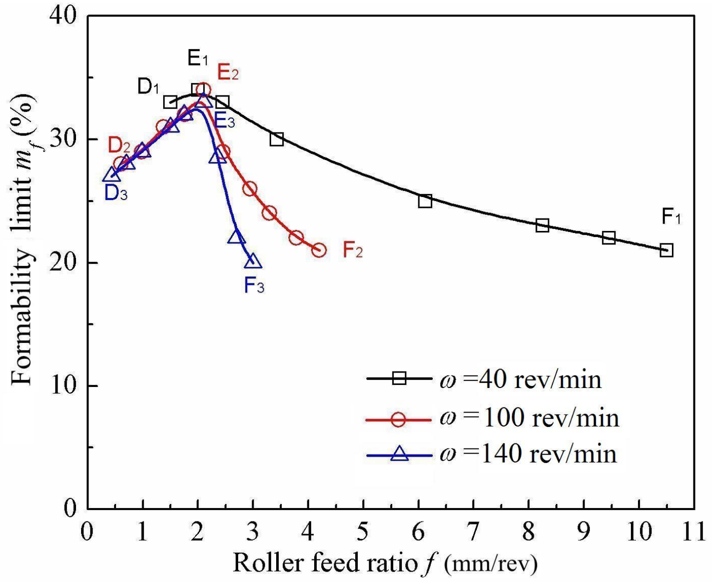

Fig. 18 Effect of the roller feed ratio on the FL at different given mandrel rotational speeds.

3.5 Analysis on responsible factors for FL

Based on the observations of the kinematic effects of the mandrel and roller on FL in Section 3.4, it is seen that under different kinematic parameters of mandrel and roller, the FL shows a single-peak distribution with the increase of roller feed ratio (Figs. 17 and 18). It is also observed that the FL shows a larger difference with different mandrel rotational speeds when the roller feed ratio is larger than 2 mm/rev (Fig. 18). These phenomena indicate that there may exist different responsible factors for the variation characteristics of the FL with the roller feed ratio. Therefore, the reasons behind these variation characteristics of the FL were analyzed in this section. Firstly, the stress triaxiality and tensile plastic strain at fracture onset under the kinematic effects of mandrel and roller were investigated. Then, the stress triaxiality and tensile plastic strain before fracture at the same roller feed depth were analyzed to clarify their contributions to the FL increase and decrease trends, respectively.

3.5.1 Stress triaxiality and strain at fracture onset

Based on the simulation results got in Sections 3.2-3.4, the variations of stress triaxiality and tensile plastic strain at fracture onset with the mandrel rotational speed, the roller feed speed and the roller feed ratio are given in Fig. 19. As seen in Fig. 19(a), at a given roller feed speed, with the increasing mandrel rotational speed, the tensile plastic strain increases, and the stress triaxiality decreases. From Fig. 19(b), it is observed that at a given mandrel rotational speed, with the increasing roller feed speed, the variation rules of stress triaxiality and tensile plastic strain are opposite to those in Fig. 19(a). From these two figures, it can be seen that the variation in the movement speed of roller or mandrel also has a significant effect on the variation of the stress triaxiality and tensile plastic strain at fracture onset with the speed of mandrel or roller. With the increase of given roller feed speed, the stress triaxiality increases, and the tensile plastic strain decreases (Fig. 19(a)). While with the increasing given mandrel rotational speed, the stress triaxiality decreases and tensile plastic strain increases (Fig. 19(b)), which are opposite to those in Fig. 19(a).

Nevertheless, this significant effect of the movement speed of roller or mandrel on the stress triaxiality and tensile plastic strain at fracture is not observed in the variations of them with the roller feed ratio, as seen in Fig. 19(c) and (d). In these two figures, the variations of stress triaxiality at fracture with the roller feed ratio under various roller feed speeds and mandrel rotational speeds are in good agreement, so do the variations of tensile plastic strain at fracture. With the increasing roller feed ratio, the stress triaxiality varies in the range of 0.4-0.9 with the rapid increase under a low roller feed ratio range (0.1-1 mm/rev) and slow increase within a wide roller feed ratio range (1-10.5 mm/rev). While with the increasing roller feed ratio, the tensile plastic strain at fracture varies in the range of 0.5-0.8 with the rapid decrease under the same low roller feed ratio range and slow decrease within the wide roller feed ratio range.

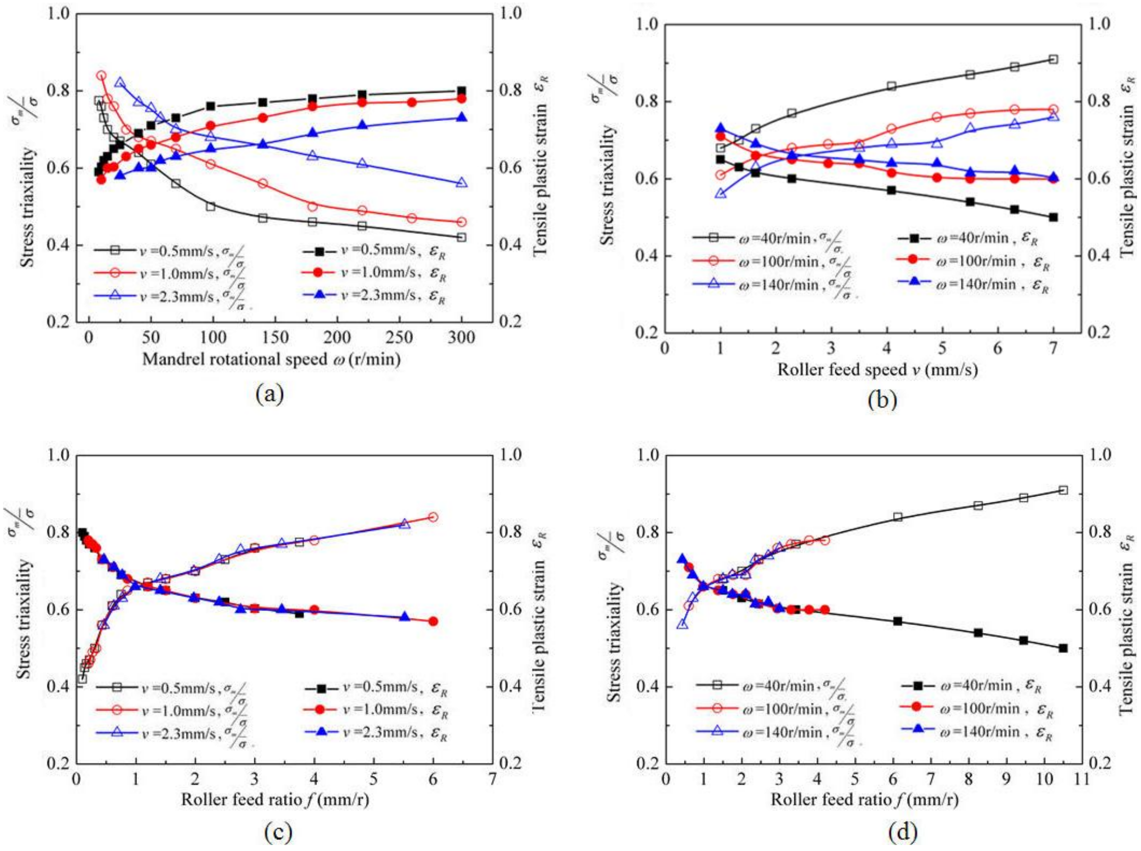

(a) (b)

(c) (d)

Fig. 19 Variations of stress triaxiality and tensile plastic strain at fracture onset (a) with the mandrel rotational speed at different given roller feed speeds, (b) with the roller feed speed at different given mandrel rotational speeds, (c) with the roller feed ratio at different given roller feed speeds and (d) with the roller feed ratio at different given mandrel rotational speeds.

One step further, the values of stress triaxiality and tensile plastic strain at fracture onset under a given roller feed ratio of 2 mm/rev with different mandrel rotational and roller feed speeds are given in Fig. 20(b). From the figure, it is seen that the stress triaxiality and tensile plastic strain keep constant whatever the mandrel rotational and roller feed speeds are. This is due to that as the roller feed ratio is given, the splitting spinning processes will experience the same roller trace, thus the same forming history whatever the mandrel rotational and roller feed speeds are. In addition, to cover the above variation range of stress triaxiality (0.4-0.9), the values of stress triaxiality and tensile plastic strain at fracture onset within a roller feed ratio range of 0.1-10.5 mm/rev are given and compared with those in different tensile tests (different stress triaxiality state), as shown in Fig. 20(b). From the figure, a dropping tendency of tensile plastic strain with stress triaxiality is observed in the splitting process, which is correspondent to that obtained from different tensile tests. While the variation curves from the splitting spinning process is higher than that from the tensile tests. The variation of the tensile plastic strain at fracture onset in the splitting spinning process is close to the range of the shear induced tensile test, and the variation of the stress triaxiality at fracture onset in the process is within the range of tensile tests with smooth round bar and notch round bar. These variation characteristics indicate that the fracture in the splitting spinning process is characteristic of the one under the high stress triaxiality level.

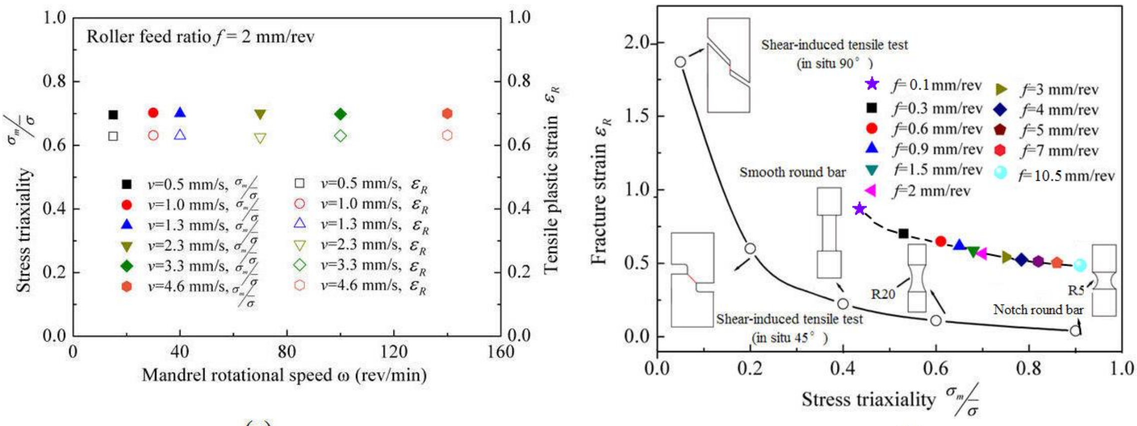

(a) (b)

Fig. 20 Stress triaxiality and tensile plastic strain at fracture onset (a) under *f* =2 mm/rev at different mandrel rotational and roller feed speeds and (b) under various tensile tests and roller feed ratios.

3.5.2 Responsible factor for FL increase

From the study in Section 3.4, it is known that when the roller feed ratio is below the critical value ($f < f_c$=2 mm/rev), the FL increases with the roller feed ratio. This increase phenomenon occurs under two conditions. One is under the small roller feed ratio below the critical value with the constant roller feed speed (in the following statement, this condition was simplified as the small roller feed ratio condition with the constant roller feed speed), as shown by C_1B_1, C_2B_2 and C_3B_3 in Fig. 17. The other is under the small roller feed ratio below the critical value with the constant mandrel rotational speed (similarly, this condition was simplified as the small roller feed ratio condition with the constant mandrel rotational speed), as shown by and D_1E_1, D_2E_2 and D_3E_3 Fig. 18. To explore the reason behind this increase of FL, the distributions of tensile plastic strain, stress triaxiality and damage value in the deformed area at three representative roller feed ratios for each condition (f=0.33, 0.43 and 0.6 mm/rev for the small roller feed ratio condition with the constant roller feed speed, while f=0.6, 0.9 and 1.8 mm/rev for the roller feed ratio condition with the constant mandrel rotational speed) were investigated under a same feed depth of 20mm, as shown in Figs. 21 and 22.

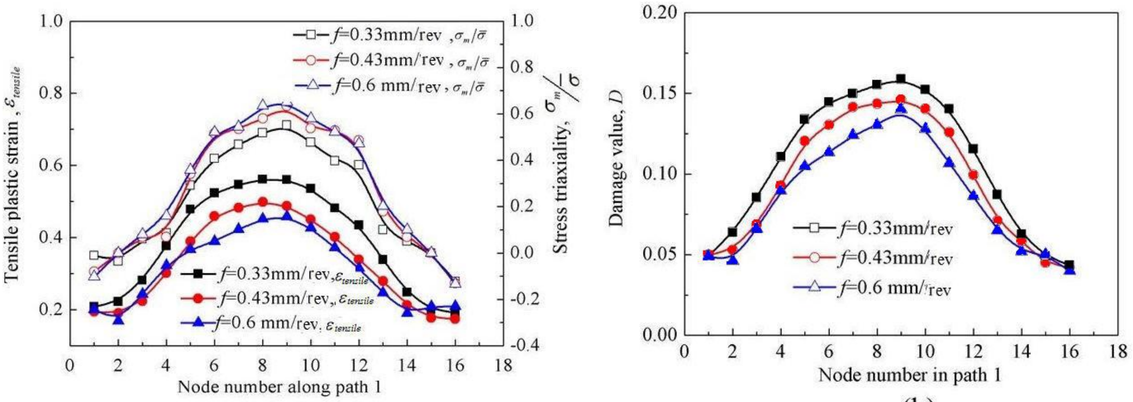

(a) (b)

Fig. 21 Effects of roller feed ratio on the distributions of (a) tensile plastic strain and stress triaxiality and (b) the damage along path 1 under the small roller feed condition with constant roller feed speed (v= 1 mm/s) and d =20 mm.

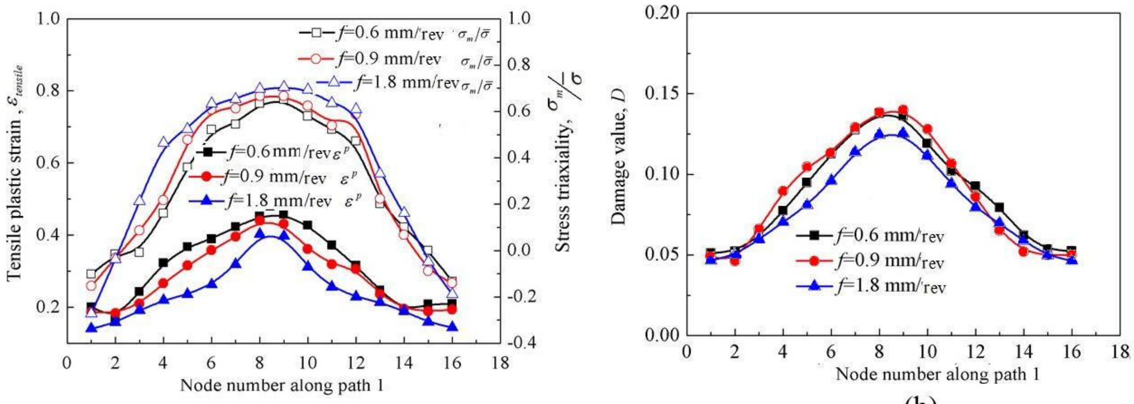

(a) (b)

Fig. 22 Effects of roller feed ratio on the distributions of (a) tensile plastic strain and stress triaxiality and (b) the damage along path 1 under the small roller feed condition with the constant mandrel rotational speed (ω = 100 rev/min) and d =20 mm.

For the small roller feed ratio condition with the constant roller feed speed, as seen from Fig. 21(a), with the increase of roller feed ratio, the stress triaxiality increases, while the tensile plastic strain decreases. To investigate the reason leading to the opposite variation in the stress triaxiality and the tensile plastic strain under this condition, sketches of the material compressed by roller, deformation area at various roller feed ratios with the constant roller feed speed and roller feed depth are given in Figs. 23. As seen in Fig. 23(a), with the increase of roller feed ratio under this condition, the feed depth per revolution increases, while the material compressed by roller decreases. The increase in the feed depth per revolution means the increase in the material in front of the roller, thus leads to an increase in resistance (Huang et al., 2008c) and results in an increase in stress triaxiality. The decrease of the material compressed by roller results in a decreasing deformed material, which leads to the decreases of deformation. Furthermore, from Fig. 23(b), it can be observed that with the increasing roller feed ratio, the contact area between the blank and roller increases. This increase further hinders the material flow to the deformed area on one hand. On the other hand, increasing roller feed ratio at the same time keeping the roller feed speed constant means the decrease of mandrel rotational speed, which would also slow the material flow to the deformed area, as shown in Fig. 24. In summary, for the small roller feed ratio condition with the constant roller feed speed, both of the decrease in deformed material and material flow velocity leads to the decrease of tensile plastic strain with the increasing roller feed ratio.

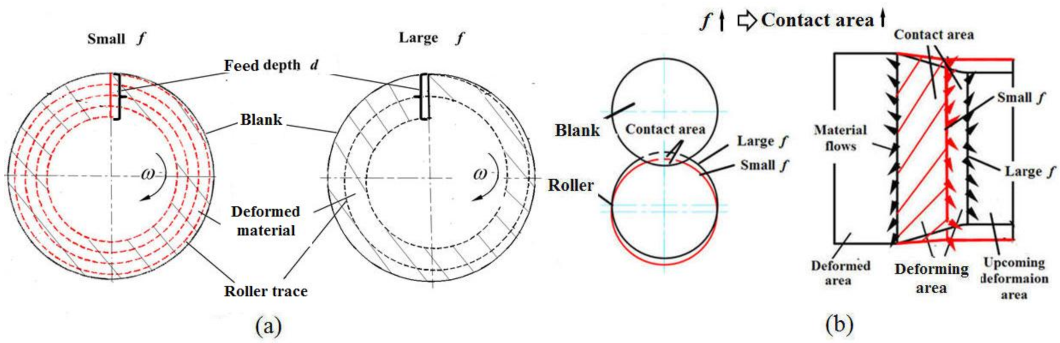

(a) (b)

Fig. 23 Sketch of (a) material compressed by roller and (b) deformation area under constant roller feed speed at various roller feed ratios with constant roller feed depth.

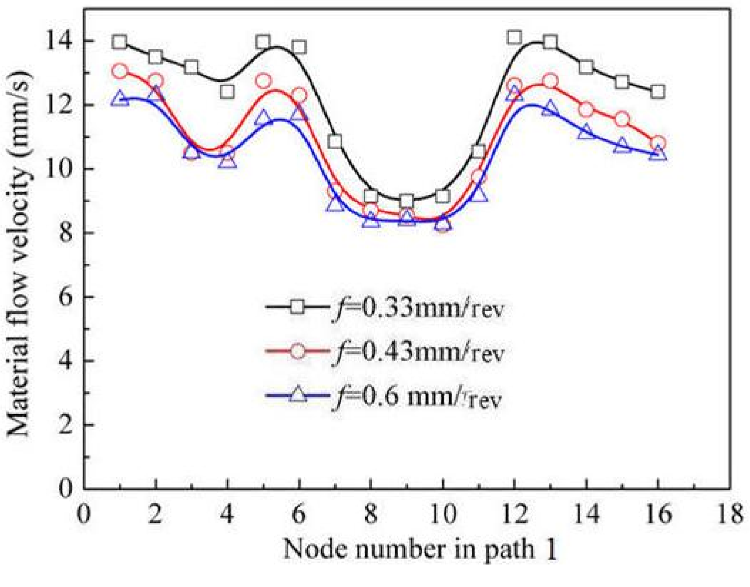

Fig. 24 Material flow velocities at various roller feed ratios.

From Fig. 21(b), it can be seen that the damage decreases with the roller feed ratio increasing, which is the same as the variation of tensile plastic strain, while opposite to the variation of stress triaxiality in Fig. 20(a). These variation rules mean that under the small roller feed ratio condition , the worsened effect on the fracture due to the increase in the stress triaxiality is weaker than the improved effect on the fracture due to the decrease in the tensile plastic strain, though the fracture is the combined effects of tensile plastic strain and stress triaxiality. Therefore under this condition, the damage evolution is more closely related to the variation of tensile plastic strain, and the responsible factor for the increase of FL with roller feed ratio increasing is the decrease of tensile plastic strain.

For the small roller feed ratio condition with the constant mandrel rotational speed a, as seen from Fig. 22, the stress triaxiality increases, while the tensile plastic strain and damage decrease with the increase in the roller feed ratio. Furthermore, under this condition, the deformed material decreases with the increasing roller feed ratio (Fig. 23 (a)), while the feed depth per revolution and the contact area both increase with the roller feed ratio (Fig. 23(b)). All these variations are the same as those under the small roller feed ratio condition with the constant roller feed speed. In addition, under the constant mandrel rotational speed, the roller feed speed also increases with the roller feed ratio increasing. The increase in roller feed speed would accelerate material flow to the deformed area at some degree. While under this condition, the roller feed ratio is not too large (below 2 mm/rev), the acceleration effect is rather limited. Thus, as a whole, the material flow velocity still decreases with the increasing roller feed ratio (Fig. 25) and leads to the decreasing tensile plastic strain under the same roller feed depth. Therefore, it can be concluded that under the small roller feed ratio condition with the constant mandrel rotation speed, the decreasing tensile plastic strain is also responsible for the increasing trend of the FL with the roller feed ratio.

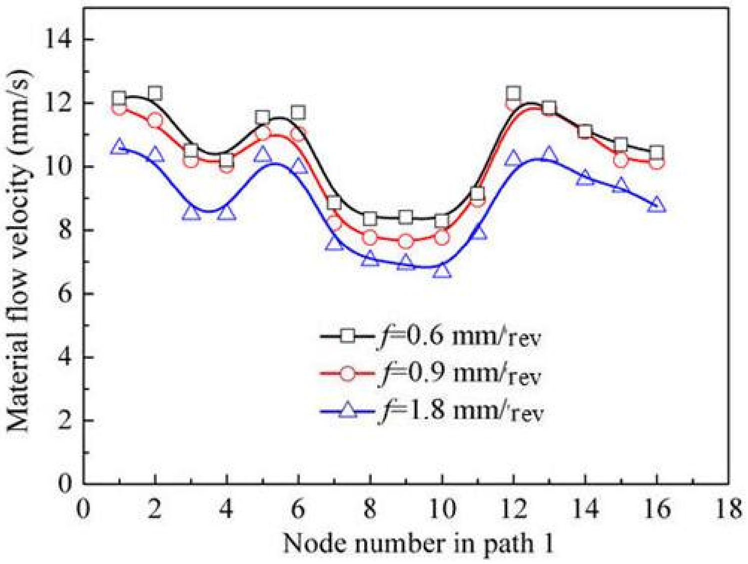

Fig. 25 Material flow velocity under small roller feed ratio condition with constant mandrel rotational speed.

3.5.3 Responsible factor for FL decrease

When the roller feed ratio is over the critical value ($f \geq 2$ mm/rev) at the given roller feed speed, the FL is observed to decrease with the increase of roller feed ratio, as shown by B_1A_1, B_2A_2 and B_3A_3 in Figs. 15 and 17. In order to explore the reasons behind the change rules of FL, the distributions of stress triaxiality, tensile plastic strain and damage at two representative roller feed ratios ($f = 2$ mm/rev and 4 mm/rev) under the same roller feed depth of 20 mm are shown in Figs. 26 and 27, respectively. Comparing these two figures, it can be seen that, the damage increases with the roller feed ratio, which is the same as stress triaxiality, while opposite to the tensile plastic strain. The reason which leads to the opposite variation of stress triaxiality and tensile plastic strain with the roller feed ratio is also the same as that under the small roller feed ratio condition with the constant roller feed speed. However, the worsened effect on the fracture due to the increase in the stress triaxiality under the large roller feed ratio is stronger than the improved effect on the fracture due to the decrease in the tensile plastic strain. Therefore, under the large roller feed ratio condition, the damage evolution is more closely related to the variation of stress triaxiality, and the increasing stress triaxiality is responsible for the decrease of the FL with the increasing roller feed ratio.

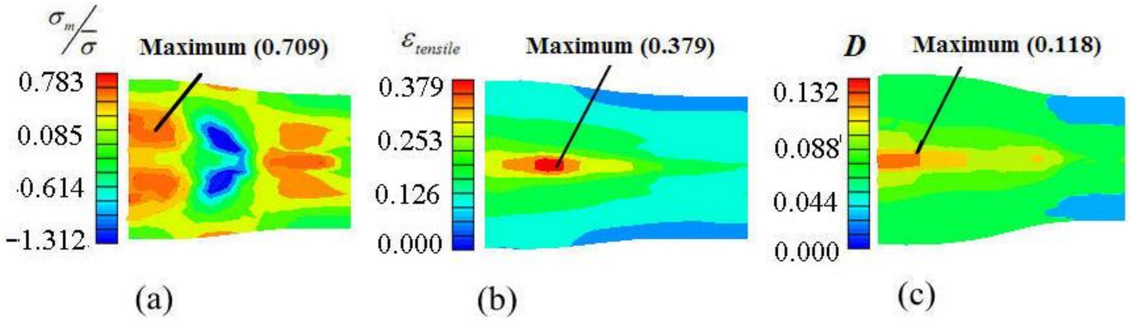

Fig. 26 Distribution of (a) stress triaxiality, (b) tensile plastic strain and (c) damage when f= 2 mm/rev, v=1 mm/s and d=20 mm.

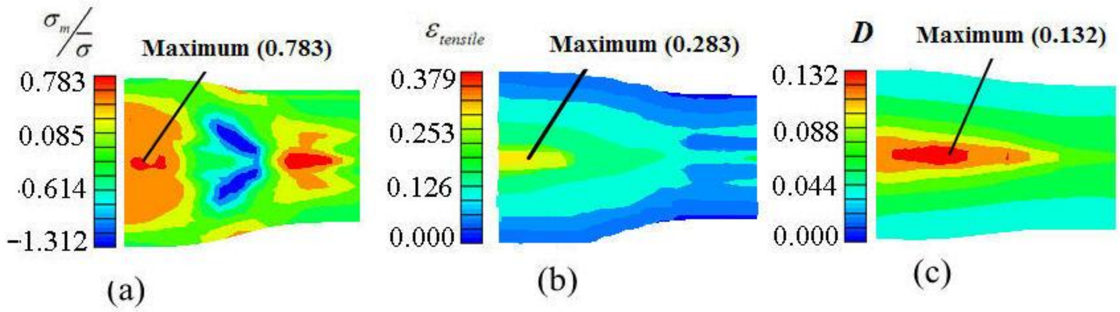

Fig. 27 Distribution of (a) stress triaxiality, (b) tensile plastic strain and (c) damage when f=4 mm/rev, v=1 mm/s and d =20 mm.

Similar to the large roller feed ratio condition, the FL under the large roller feed ratio but with the constant mandrel rotation speed also decreases with the roller feed ratio, as shown by E_1F_1, E_2F_2 and E_3F_3 in Figs. 16 and 18. To find the reasons behind this decrease of FL, the distributions of stress triaxiality, tensile plastic strain and damage at two representative roller feed ratios (f=2.0 and 4.5 mm/rev) under the same roller feed depth of 20 mm are shown in Figs. 28 - 29.

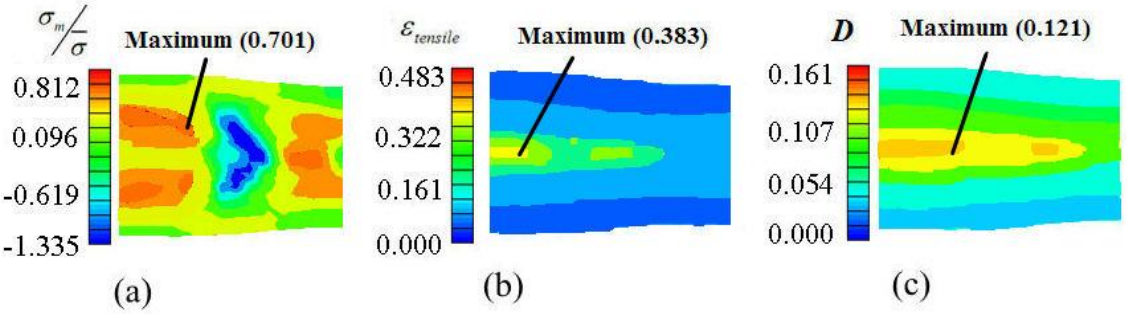

Fig. 28 Distribution of (a) stress triaxiality, (b) tensile plastic strain and (c) damage when f=2.0 mm/rev, ω=40 rev/min and d= 20 mm.

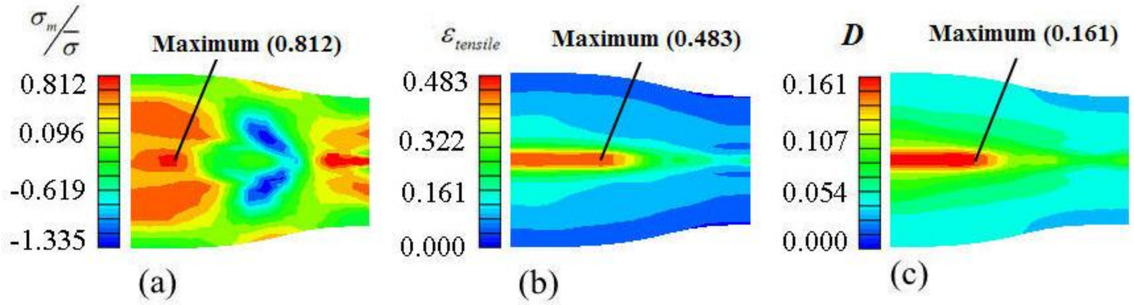

Fig. 29 Distribution of (a) stress triaxiality; (b) tensile plastic strain and (c) damage when f=4.5 mm/rev, ω=40 rev/min and d= 20 mm.

As seen in Figs. 28 and 29, the stress triaxiality and tensile plastic strain both increase with the roller feed ratio, so does the damage. As mentioned in Section 3.5.2, the increasing stress triaxiality with the roller feed ratio is mainly attributed to the increasing deformation resistance in front of the roller. While for the material flow, both the hindering effect and the acceleration effect exist resulting from the increase in the contact area and the roller feed speed, which is caused by the increasing roller feed ratio condition under the constant mandrel rotational speed. While under this condition, the roller feed ratio is large (over 2 mm/rev), the acceleration effect becomes stronger and leads to material flow velocity increase with the roller feed ratio, as shown in Fig. 30. The increasing material flow velocity is helpful for material to flow to the deformed area, which results in the increase of tensile plastic strain under the same roller feed depth though the deformed material decreases with the increasing roller feed ratio (Fig. 23(a)). As the increase in stress triaxiality and tensile plastic strain both leads to damage onset, it can be concluded that under the large roller feed ratio condition with the constant mandrel rotation speed, the responsible factor for the decrease of FL with the increasing roller feed ratio is the simultaneous increase of stress triaxiality and tensile plastic strain .

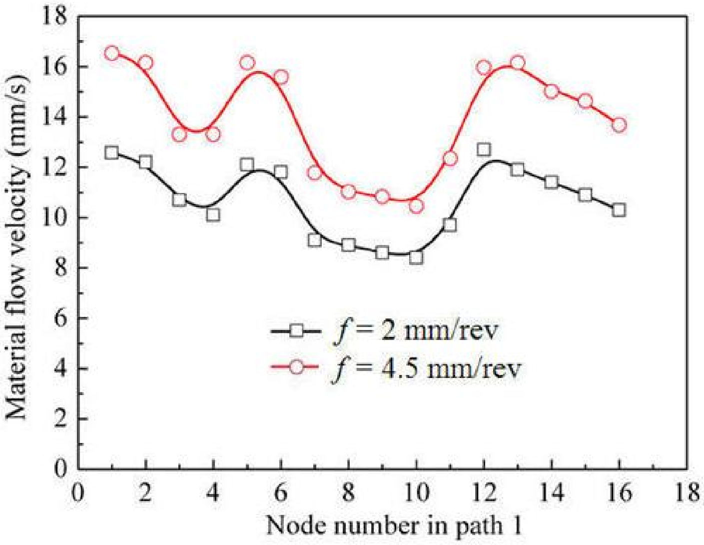

Fig. 30 Material flow velocity with *f* ≥2 mm/rev under the constant mandrel rotational speed.

It also needs to be noted that, when the roller feed ratio is larger than the critical value (*f* ≥2 mm/rev), the FL decreases remarkably with the increase of mandrel rotational speed, as shown in Fig. 18. To explore the source leading to the decrease, the distribution of the material flow velocity, tensile plastic strain, stress triaxiality and damage under a given roller feed ratio (*f* =3 mm/rev) under the same roller feed depth of 20 mm but different mandrel rotational speeds (40, 100 and 140 rev/min) are shown in Figs. 31-34. As seen from Fig. 31, the material flow velocity under the large mandrel rotational speed are much larger than that under the small mandrel rotational speed. This is due to that, under the constant roller feed ratio, the increases of mandrel rotational speed means the proportional increase of the roller feed speed. The simultaneous increase of the mandrel rotational and roller feed speeds leads to obvious increase of kinematic effect of mandrel and roller, which results in the increase of material flow velocity. This large material flow velocity means more material flows to the deformed area, thus resulting in a large tensile plastic strain under the same roller feed depth (Fig. 32). While from Fig. 33, it can be seen that the stress triaxiality in the deformed area shows no big difference due to the same roller feed ratio. The increase of tensile plastic strain leads to the larger damage appears for large mandrel rotational speed, as shown in Fig. 34, and thus finally resulting in a smaller FL.

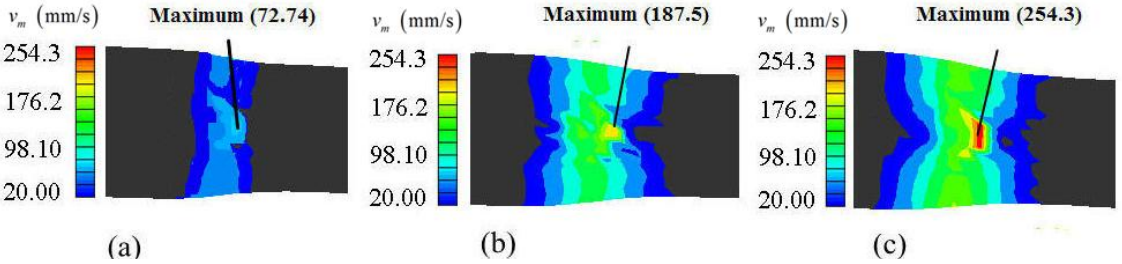

Fig. 31 Distribution of material flow velocity under *f* =3 mm/rev at *d*= 20mm: (a) 40 rev/min, (b) 100 rev/min and (c) 140 rev/min.

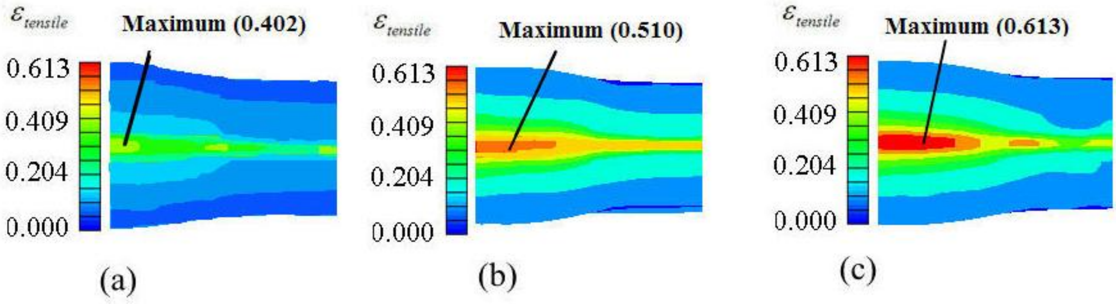

Fig. 32 Distribution of tensile plastic strain under *f* =3 mm/rev at *d*= 20mm: (a) 40 rev/min, (b) 100 rev/min and (c) 140 rev/min.

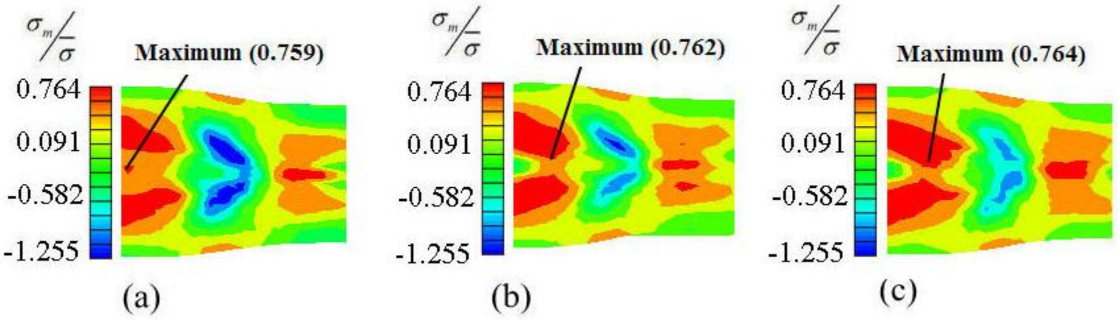

Fig. 33 Distribution of stress triaxiality under *f* =3 mm/rev at *d*= 20mm: (a) 40 rev/min, (b) 100 rev/min and (c) 140 rev/min..

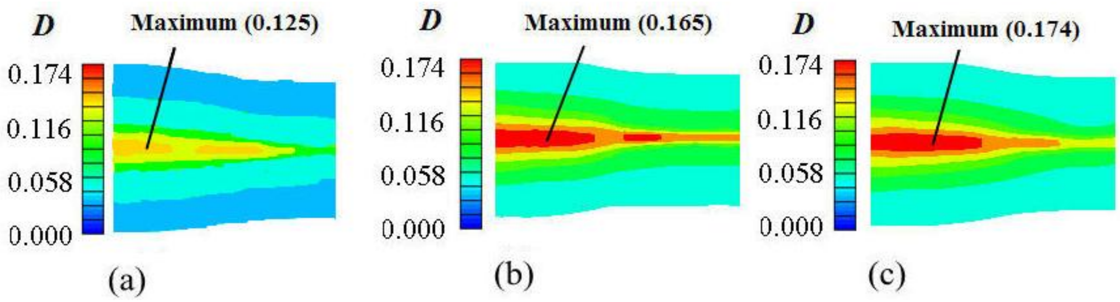

Fig. 34 Distribution of damage under f=3 mm/rev at d= 20mm: (a) 40 rev/min, (b) 100 rev/min and (c) 140 rev/min..

4. Identification of process window

Based on the investigations on the kinematic effects of the mandrel and roller on the FL, the process window of mandrel and roller is identifies to extend the FL in the splitting spinning process. In the process, the requirement of FL is often larger than 30%. Based on this requirement, the roller feed ratio was determined firstly. From Fig. 17, it can be seen that a roller feed ratio within 1-3.5 mm/rev could meet this requirement at the three given roller feed speeds. While in Fig. 18, it is observed that the FL under a large mandrel rotational speed of 140 rev/min decreases faster and is much smaller than those under small mandrel rotational speeds (40 and 100 rev/min) when $f \geq 2$ mm/rev. Thus, the mandrel rotational speed was determined to be no larger than 100 rev/min, and the roller feed ratio range of 1-2.5 mm/rev could satisfy the requirement under other two mandrel rotational speeds of 40 and 100 rev/min. Combining the intersection of the roller feed ratio range, the roller feed ratio within 1-2.5 mm/rev is appropriate. Furthermore, the closer to the critical value of the roller feed ratio (2 mm/rev) is, the larger the FL is.

However, just determining the roller feed ratio is not enough for the process window as the FL also varies with the forming speeds. Therefore, the process window of the roller feed and mandrel rotational speeds were also obtained. As seen in Fig. 15, the requirement of FL can be met with the roller feed speed range of 0.5-2.3 mm/s and the mandrel rotational speed within 8-140 rev/min. As talked above, the mandrel rotational speed was determined to be no larger than 100 rev/min. Thus, the mandrel rotational speed range of 8-100 rev/min is suitable. In addition, as observed in Fig. 16, with the mandrel rotational speed of 40 and 100 r/min, the roller feed speed was determined within 1- 4 mm/s to meet the requirement. Considering the roller feed speed range (0.5-2.3 mm/s) got in Fig. 15, the roller feed speed within 0.5-4 mm/s is appropriate.

In summary, the process window for the large FL over 30% was obtained as follows: the roller feed ratio, mandrel rotational speed and roller feed speed should be within 1-2.5 mm/rev, 8-100 rev/min and 0.5-4 mm/s, respectively, and f=2 mm/rev should be maintained as close as possible.

5. Experiments

The splitting spinning experiments with the roller feed ratio 1 mm/rev (ω =60 rev/min, v=1 mm/s) and 3 mm/rev (ω =100 rev/min, v=5 mm/s) were conducted as case studies in this research. The disk blank dimensions and other process parameters in the experiments were the same as those given in Table 3. The experiments were carried out on a CZ900/2CNC spinning machine, as shown in Fig. 35. To make the tube blank rotate synchronously with the mandrel, the tailstock was forced to press the end surfaces of blank. The blank surface was coated with MoS_2 as lubricant. Furthermore, a coolant was also used throughout the experiment process to avoid a rapid temperature rise in the spun part.

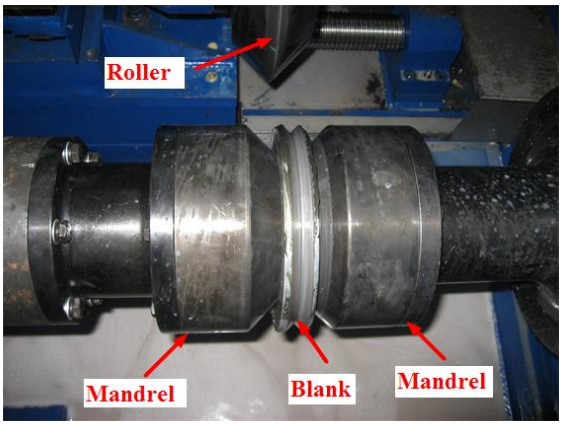

Fig. 35 Experimental setup of splitting spinning.

The thickness distribution along the flange (It is defined by 6 measurement positions along the direction indicated by the arrow in Fig. 37) in the experiments at the feed depth of 12 mm and 24 mm under the roller feed ratio of 1 mm/rev are shown in Fig. 36. The thickness of the spun parts by experiment was measured by an ultrasonic thickness meter in the 6 positions. While the thickness of the spun parts by simulation was got based on node coordinate in the same positions as those in experiment by calculating the distances of these nodes to the parts' outer surfaces. In Fig. 36, it is observed that the spun parts in the experiments and simulations have the similar profiles. The flange thicknesses in the simulations also show a similar trend as those in the experiments. The maximum difference between simulations and experiments is 11.2%, which appears at the feed depth of 24 mm. The flange thicknesses under the feed depth of 12 mm are observed to be larger than that the feed depth of 24 mm. This is because the outer surfaces of deformed flanges under the feed depth of 12 mm do not contact with mandrels. The flange cannot be formed into the desired shape, leading to the thickness larger than 10 mm. While under the feed depth of 24 mm, the outer surfaces of the deformed flanges contact mandrels and the flanges are formed into the desired shape with the thickness of approximately 10mm (Huang et al., 2009). These comparisons show that the splitting spinning FE model established in this study is appropriate to reveal the forming characteristic in the splitting spinning process.

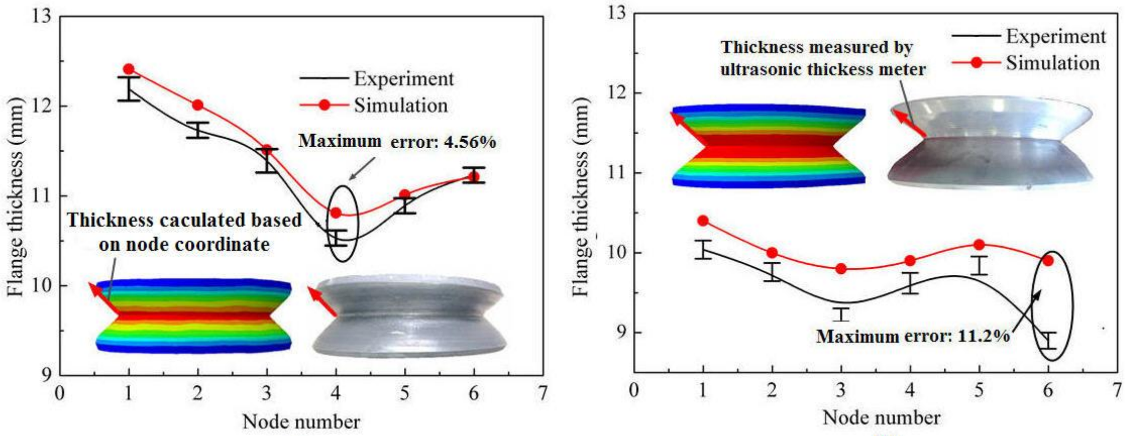

(a)

(b)

Fig. 36 Profiles and flange thickness distributions in experiments and simulations under the roller feed ratio of 1 mm/rev at (a) feed depth 12 mm and (b) feed depth 24 mm.

Furthermore, fracture was also observed in experiments under the roller feed ratio of 3 and 1 mm/rev. Fig. 37 shows that all the fractures appear in the flange bottom area under both of the roller feed ratios. To accurately calculate the feed depth at fracture onset, the fracture was analyzed under the microscope view in 3 positions, including two ends (E1 and E2) and middle (M) of the fracture, as shown in Fig. 38. As seen in this figure, the morphology at E1 position exists numbers of dimple and shows ductile fracture characteristic (Fig. 38(a)), while at M and E2 positions, they appear less dimples combined with small and smooth flat and show intergranular fracture characteristic (Fig. 38(b) and (c)). As well known, the fracture onset position shows ductile fracture behavior, while the fracture propagation position shows intergranular fracture behavior (Li et al., 2016). Thus the fracture onset position in the experiment was determined as E1 position, and then the feed depth can be accurately calculated. When the roller feed ratio is 3 mm/rev, the fracture appears in the experiment with the critical feed depth of 26.4 mm while the critical feed depth predicted by the simulation is 26 mm. At the roller feed ratio of 1 mm/rev, the fracture in the experiment appears as the critical feed depth reaches 31.2 mm and the prediction by the simulation is 31 mm. Considering the small difference between the critical feed depths in the simulations and experiments, it can be concluded that the FE model established in this study, coupled with the modified Lemaitre criterion is able to accurately predict the fracture occurrence and FL in the splitting spinning process.

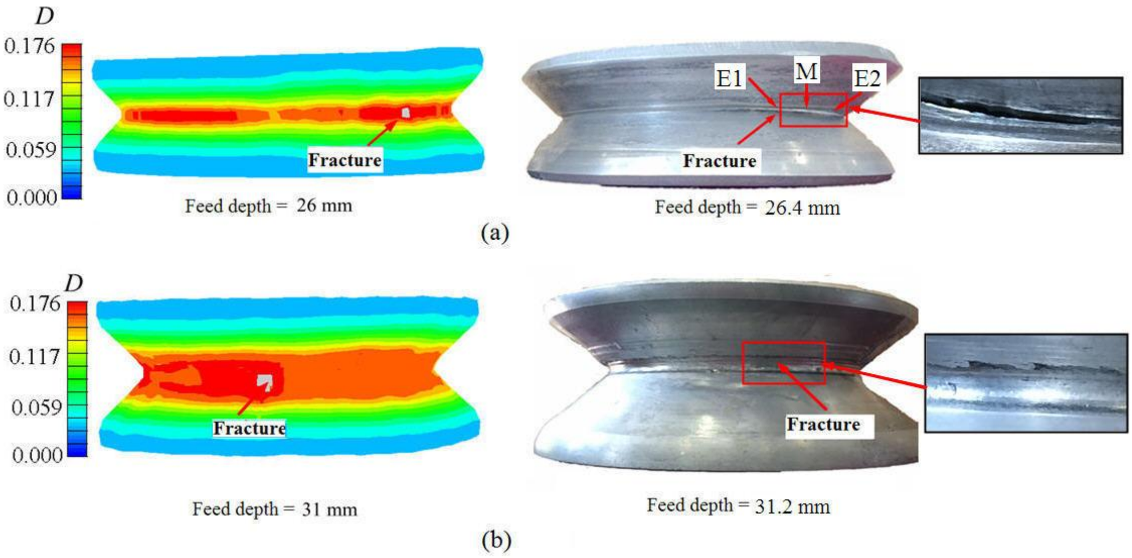

Fig. 37 Feed depths when fracture appears in experiment and simulation under different roller feed ratios: (a) 3 mm/rev and (b) 1 mm/rev.

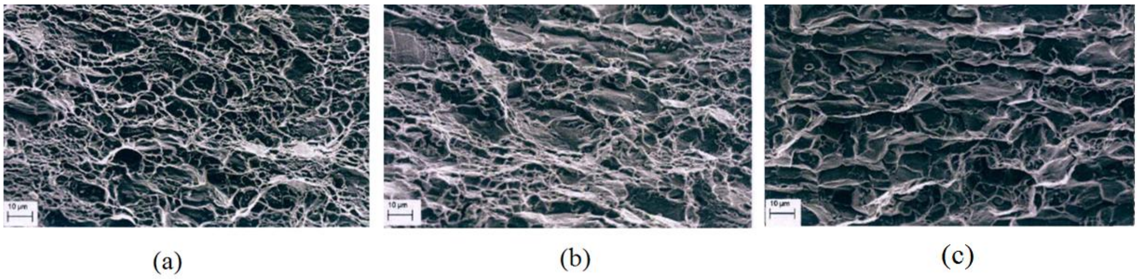

Fig. 38 Fracture morphology on three positions (a) one end of the fracture (E1), (b) middle of the fracture (M) and (c) the other end of the fracture (E2).

According to the process window about the mandrel and roller determined in Section 4, three splitting spinning experiments with the feed depth of 32 mm under the roller feed ratio of 2 mm/rev (ω=30 rev/min with v=1 mm/s, ω=60 rev/min with v=2 mm/s, ω=90 rev/min with v=3 mm/s) were conducted, as shown in Fig. 39. It is clearly observed that the spun parts without fracture were obtained at the roller feed ratio of 2 mm/rev under the three different combinations of mandrel rotation and roller feed speeds. These results indicate that the process window are reliable to get a high FL larger than 32%.

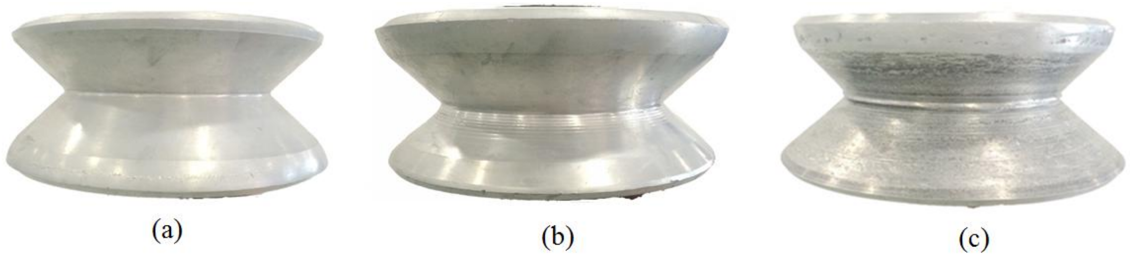
(a) (b) (c)

Fig. 39 Spitting spun parts when roller feeds 32 mm under a roller feed ratio of 2 mm/rev with various mandrel rotation speeds and roller feed speeds: (a) ω = 30 rev/min and v=1 mm/s, (b) ω = 60 rev/min and v=2mm/s and (c) ω = 90 rev/min and v=3 mm/s.

6. Conclusions

The FL characteristics and change reasons of the 5A02-O aluminium alloy in splitting spinning considering the kinematic effect of the mandrel and roller were investigated using the FE simulation with a built-in modified Lemaitre criterion and physical experiment. The following concluding remarks are thus drawn:

(1) The FL initially increases and then decreases with an increasing mandrel rotational speed, whereas the maximum FL decreases slightly and appears at the larger mandrel rotational speed when the given roller feed speed increases. In addition, the FL under different given mandrel rotational speeds varies with the roller feed speed in almost the same way as the variation of mandrel rotational speed.

(2) Using the roller feed ratio as a process variable to reveal the combined effect of mandrel rotational and roller feed speeds, the FL is seen to initially increase and then decrease with increasing roller feed ratio, and the decrease in FL becomes more remarkable with the mandrel rotational speed increasing. The FL reaches its peak value at a critical feed ratio of approximately 2 mm/rev independent of the mandrel rotational and the roller feed speeds.

(3) With the increasing roller feed ratio, the stress triaxiality at fracture onset increases

while the tensile plastic strain at fracture onset decreases, and they show little difference with the variations of the roller feed and mandrel rotational speeds.

(4) When the roller feed ratio is less than the critical value, the increase of FL with the increase of roller feed ratio is mainly due to the decreasing tensile plastic strain cause by the decreasing deformed material and material flow velocity. When the roller feed ratio is greater than the critical value, with the increase of roller feed ratio under the constant roller feed speed, the decrease of FL is mainly due to the increasing stress triaxiality resulting from the increasing material resistance, while under the constant mandrel rotational speed, the decrease of FL is due to the simultaneous increase of stress triaxiality and tensile plastic strain resulting from the increasing material flow velocity.

(5) To obtain high FLs greater than 30%, the process window of the mandrel and roller are determined and further verified by experiments: the roller feed ratio within 1-2.5 mm/rev, the mandrel rotational speed within 8-100 rev/min and the roller feed speed within 0.5-4 mm/s.

Acknowledgements

The authors acknowledge the funding support from the National Science Fund for Distinguished Young Scholars of China (Project 51625505), , Key Program Project of the Joint Fund of Astronomy and National Natural Science Foundation of China (Project U1537203) and Research Fund of the State Key Laboratory of Solidification Processing (Projects 97-QZ-2014 and 90-QP-2013). The authors also acknowledge the partial support of the EU FP7 Marie Curie International Research Staff Exchange Scheme (IRSES, MatProFuture, Project 318968).

References

Bonora, N., Salvini, P., lacoviello, F., 1996. Experimental identification of damage evolution law in AI-Li 2091 alloy.XXV AlAS National Meeting, Gallipoli. 345-355.

Bonora, N., 1997a. A nonlinear CDM damage model for ductile failure. Eng Fracture Mechanics, 58(1/2), 11–28.

Bonora, N., 1997b. On the effect of triaxial state of stress on ductility using nonlinear CDM model. Int. J. Fracture, 88, 359–371.

Bouchard, P.-O., Bourgeon, L., Fayolle, S., Mocellin, K., 2011. An enhanced Lemaitre model formulation for materials processing damage computation. Int. J. Mater. Form. 4, 299–315.

Chow, C.L, Wang, J., 1987. An anisotropic theory of continuum damage mechanics for ductile fracture. Eng Fracture Mechanics, 27, 547-558.

Fu, M.W., 2016. Design and Development of Metal Forming Processes and Products aided by Finite Element Simulation, first ed. Springer-Verlag London Ltd.

Groche, P., Ringler, J., Vucic, D., 2007a. New Forming Processes for Sheet Metal with Large Plastic Deformation. Key. Eng. Mater. 344, 251–258.

Groche, P., Vucic, D., Jöckel, M., 2007b. Basics of linear flow splitting. J. Mater. Process. Technol. 183, 249–255.

Grotmann. D., 1990. Untersuchungen zum rotationskinematischen Umformen von Profilscheiben. Diss. University Siegen.

Hauk, S., Vazquez, V.H., Altan, T., 2000. Finite element simulation of the Flow-Splitting-Process. J. Mater. Process. Technol. 98, 70–80.

Huang, L., Yang, H., Zhan, M., 2008a. 3D-FE modeling method of splitting spinning. Comput. Mater. Sci. 42, 643–652.

Huang, L., Yang, H., Zhan, M., Hu, L., 2008b. Numerical simulation of influence of material parameters on splitting spinning of aluminum alloy. T. Nonferr. Metal. Soc 2008. 18, 674-681.

Huang, L., Yang, H., Zhan, M., Liu, Y., 2008c. Analysis of splitting spinning force by the principal stress method. J. Mater. Process. Technol. 201, 267–272.

Huang, L., Yang, H., Zhan, M., Hu, L., 2009. Forming characteristics of splitting spinning based on the behaviors of roller. Comput. Mater. Sci. 45, 449–461.

Huang, L., Zeng, R., Zhang, X., Li, J., 2014. Study on plastic deformation behavior of hot splitting spinning of TA15 titanium alloy. Mater. Des. 58, 465–474.

Kabirian, F., Khan, A.S., Pandey, A., 2014. Negative to positive strain rate sensitivity in 5xxx series aluminum alloys: Experiment and constitutive modeling. Int. J. Plast. 55, 232–246.

Ko, Y.K., Lee, J.S., Huh, H., Kim, H.K., Park, S.H., 2007. Prediction of fracture in hub-hole expanding process using a new ductile fracture criterion. J. Mater. Process. Technol. s 187–188, 358–362.

Lemaitre, J., 1985. A continuous damage mechanics model for ductile fracture. J. Eng. Mat. Tech. 107, 83-89.

Li, B., Wang, X., Chen, H., Hu, J., Huang, C., Gou, G., 2016. Influence of heat treatment on the strength and fracture toughness of 7N01 aluminum alloy. J. Alloy. Compd. 678, 160-166.

Li, H., Fu, M.W., Lu, J., Yang, H., 2011. Ductile fracture: Experiments and computations. Int. J. Plast. 27, 147–180.

Liu, H., Yang, Y., Yu, Z., Sun, Z., Wang, Y., 2009. The application of a ductile fracture criterion to the prediction of the forming limit of sheet metals. J. Mater. Process. Technol. 209, 5443–5447.

Ma, H., Xu, W., Jin, B., Shan, D., Nutt, S.R., 2015. Damage evaluation in tube spinnability test with ductile fracture criteria. Int. J. Mech. Sci. 100, 99-111.

Malcher, L., Mamiya, E.N., 2014. An improved damage evolution law based on continuum damage mechanics and its dependence on both stress triaxiality and the third invariant. Int. J. Plast. 56, 232–261.

Mashayekhi, M., Ziaei-Rad, S., Parvizian, J., Niklewicz, J., Hadavinia, H., 2007. Ductile crack growth based on damage criterion: Experimental and numerical studies. Mech. Mater. 39, 623–636.

Mirnia, M.J., Shamsari, M., 2017. Numerical prediction of failure in single point incremental forming using a phenomenological ductile fracture criterion. J. Mater. Process. Technol. 244, 17–43.

Müller, C., Bohn, T., Bruder, E., Bruder, T., Lersheim, V., El, D.C., Groche, P., Veleva, D., 2007. Severe plastic deformation by linear flow splitting. Materwiss. Werksttech. 38, 842-854.

Packham. C., 1978. Manufacture of one piece sheet metal V-pullys with up to three grooves. Sheet. Met. Ind. 55, 441-445.

Ran, J.Q., Fu, M.W., 2014. A hybrid model for analysis of ductile fracture in micro-scaled plastic deformation of multiphase alloys. Int. J. Plast. 61, 1–16.

Schmitt, W., Brenneis, M., Groche, P., 2012. On the development of flexible flow splitting. Proceedings of the 14th Metal Forming Conference, Krakow, Polen.

Schmoeckel, D., Hauk, S., 2000. Tooling and process control for splitting of disk blanks. J. Mater. Process. Technol. 98, 65–69.

Shang, X., Cui, Z., Fu, M.W., 2017. Dynamic recrystallization based ductile fracture modeling in hot working of metallic materials. Int. J. Plast. doi:10.1016/j.ijplas.2017.04.002.

Song, W.J., Kim, S.W., Kim, J., Kang, B.S., 2005. Analytical and numerical analysis of bursting failure prediction in tube hydroforming. J. Mater. Process. Technol. s 164–165, 1618–1623.

Tang, B.T., Bruschi, S., Ghiotti, A., Bariani, P.F., 2016. An improved damage evolution model to predict fracture of steel sheet at elevated temperature. J. Mater. Process. Technol. 228, 76–87.

Wang, L., Long, H., Ashley, D., Roberts, M., White, P., 2011. Effects of the roller feed ratio on wrinkling failure in conventional spinning of a cylindrical cup. Proc. Inst. Mech. Eng. Part B J. Eng. Manuf. 225, 1991-2006.

Wu, J., Zhan, M., Jiang, H.B., Chen, F., Yang, H., 2011. A modified Lemaitre ductile fracture criterion and its application to spinning forming. Chinese. J. Aeronau. 32(7), 1309-1317. (in Chinese)

Xu, Z.T., Peng, L.F., Fu, M.W., Lai, X.M., 2015. Size effect affected formability of sheet metals in micro/meso scale plastic deformation: Experiment and modeling. Int. J. Plast. 68, 34–54.

Yan, Y., Wang, H.,Wan, M., 2011. Prediction of fracture in press bend forming of aluminum alloy high-stiffener integral panels. Comput. Mater. Sci. 50, 2232–2244.

Zhan, M., Gu, C., Jiang, Z., Hu, L., Yang, H., 2009. Application of ductile fracture criteria in spin-forming and tube-bending processes. Comput. Mater. Sci. 47, 353–365.

Zhao, X., Li, Z., 2016. A solution of transient rolling contact with velocity dependent friction by the explicit finite element method. Eng. Comp. 33, 1033-1050.